Simulated Electrification of a Small Thunderstorm with Two-Moment Bulk Microphysics

EDWARD R. MANSELL AND CONRAD L. ZIEGLER

NOAA/OAR/National Severe Storms Laboratory, Norman, Oklahoma

ERIC C. BRUNING

Cooperative Institute for Climate Studies, Earth System Science Interdisciplinary Center, University of Maryland, College Park, College Park, Maryland

(Manuscript received 30 September 2008, in final form 27 June 2009)

ABSTRACT

Electrification and lightning are simulated for a small continental multicell storm. The results are consistent with observations and thus provide additional understanding of the charging processes and evolution of this storm. The first six observed lightning flashes were all negative cloud-to-ground (CG) flashes, after which intracloud (IC) flashes also occurred between middle and upper levels of the storm. The model simulation reproduces the basic evolution of lightning from low and middle levels to upper levels. The observed lightning indicated an initial charge structure of at least an inverted dipole (negative charge above positive). The simulations show that noninductive charge separation higher in the storm can enhance the main negative charge sufficiently to produce negative CG flashes before upper-level IC flashes commence. The result is a ''bottom-heavy'' tripole charge structure with midlevel negative charge and a lower positive charge region that is more significant than the upper positive region, in contrast to the traditional tripole structure that has a less significant lower positive charge region. Additionally, the occurrence of cloud-to-ground lightning is not necessarily a result of excess net charge carried by the storm, but it is primarily caused by the local potential imbalance between the lowest charge regions.

The two-moment microphysics scheme used for this study predicted mass mixing ratio and number concentration of cloud droplets, rain, ice crystals, snow, and graupel. Bulk particle density of graupel was also predicted, which allows a single category to represent a greater range of particle characteristics. (An additional hail category is available but was not needed for the present study.) The prediction of hydrometeor number concentration is particularly critical for charge separation at higher temperatures ($-5° < T < -20°$C) in the mixed phase region, where ice crystals are produced by rime fracturing (Hallett–Mossop process) and by splintering of freezing drops. Cloud droplet concentration prediction also affected the rates of inductive charge separation between graupel and droplets.

1. Introduction

A small multicell storm complex with interesting lightning behavior was observed on 28–29 June 2004 during the Thunderstorm Electrification and Lightning Experiment (TELEX) (MacGorman et al. 2008). The storm was located 50 km northwest of Norman, Oklahoma, and remained stationary. Observation platforms included the KOUN polarimetric radar, a lightning mapping array (LMA), mobile radars, and soundings with electric field meters. The convection on this day was characterized by short-lived shallow cells, a few of which grew sufficiently above the freezing level to electrify strongly and produce lightning.

Analysis of polarimetric radar by Bruning et al. (2007) indicated that the warm rain (collision–coalescence) process was likely the dominant mode of initial precipitation formation and that graupel and small hail first appeared in the lightning-producing cells as a result of drop freezing. Inference from LMA-observed lightning showed an initial significant charge structure composed of main negative and lower positive charges (negative dipole) with associated negative cloud-to-ground (CG) lightning. Subsequent upper-level intracloud (IC) lightning

Corresponding author address: Edward Mansell, 120 D. L. Boren Blvd., Norman, OK 73072.
E-mail: ted.mansell@noaa.gov

DOI: 10.1175/2009JAS2965.1

indicated development of a significant upper positive charge region. A negative screening layer at cloud top was inferred from electric field meter data but was apparently not involved in lightning.

The interpretation by Bruning et al. (2007) of the observations painted a reasonable picture of the lightning and microphysics of the storm, but some aspects remained unclear, particularly the initial charge structure of the storm that produced exclusively negative cloud-to-ground (−CG) lightning flashes. Although lightning developed later in the upper part of the storm, the majority of lightning activity occurred in the lower part of the storm. The storm electrification simulation study of Mansell et al. (2005) noted that the lower altitude (higher temperature) regions of storms pose difficulties to microphysics schemes that predict only total hydrometeor mass (single moment) because ice crystal concentrations must somehow be derived to calculate charge separation rates in rebounding collisions with graupel. The present model predicts hydrometeor number concentration in addition to mass for all species, so that, for example, ice multiplication processes (splintering, Hallett–Mossop, etc.) and subsequent crystal growth can be better treated.

The low observed flash rate ($\sim$1 flash min^{-1}) allows for a detailed look at electrical evolution between lightning flashes. The small dimensions of the storm also allow simulation at high spatial resolution in a relatively small domain that avoids excessive computational requirements. The marginal flash rates, relatively low echo tops, and strongly evolving multicell morphology of the observed storm make for an interesting and challenging case for numerical modeling, both to evaluate microphysical and electrical processes and to gain further understanding of the observations.

2. Model details

Electrification physics have been merged into a new version of the Collaborative Model for Multiscale Atmospheric Simulation (COMMAS) (Wicker and Wilhelmson 1995). As described in Coniglio et al. (2006), the model uses the basic equation set from Klemp and Wilhelmson (1978b) and prognostic equations are included for momentum, pressure, potential temperature, and turbulent kinetic energy (Deardorff 1980). Time integration is performed with a third-order Runge–Kutta (RK) scheme (Wicker and Skamarock 2002). Advection on the first two RK iterations uses fifth-order upwind differencing. On the final RK step, scalar quantities (e.g., potential temperature, mixing ratio, number concentration, electric charge) are advected using a sixth-order finite difference with a monotonicity filter (Leonard 1991) and are computationally diffused (horizontal directions only) with the simple monotonic filter of Xue (2000), following Bryan (2005). Wind components, on the other hand, are advected with a fifth-order weighted essentially nonoscillatory (WENO) scheme (Jiang and Shu 1996; Shu 2003; Bryan 2005). Sedimentation uses the Kato (1995) first-order ''box-Lagrangian'' scheme.

The cloud microphysics scheme is an updated version of the one originally developed by Ziegler (1985) that predicts two independent moments (mass and number concentration) for six hydrometeor types (droplets, rain, ice crystals, snow, graupel, and hail). The original scheme was used in previous electrification studies with a kinematic model (Ziegler et al. 1986, 1991; Ziegler and MacGorman 1994). Details of the updated scheme are provided in the appendices. The updated two-moment scheme also predicts the bulk concentration of cloud condensation nuclei (CCN) as well as the average bulk densities of graupel and hail. The variable graupel density allows the single graupel category to represent a spectrum of particles ranging from high-density frozen drops (or small hail) to low-density graupel. There were no indications of large hail in this case, and test runs with the hail category activated produced only small hail ($<$4 mm) in an initial cell and essentially no hail in the strongly electrified cell. Bruning et al. (2007) did infer small hail from the radar data, but this can be adequately represented by frozen drops in the graupel category, whereas the hail category is intended to represent larger hail. The simulated storm was very sensitive to initial conditions and required a large number of experimental runs, so the hail category was omitted from the present simulations to save some computational cost.

Electrification processes (Mansell et al. 2005) include parameterizations of multiple laboratory results of noninductive charge separation in rebounding graupel–ice collisions. Small ion processes such as attachment and drift motion are treated explicitly. A set of sensitivity tests found that of the standard noninductive charge separation schemes described by Mansell et al. (2005), the schemes based on rime accretion rate (e.g., Saunders and Peck 1998) worked better than the others to reproduce the charge and lightning development from lower dipole to full tripole that was inferred from LMA observations. Better results were achieved when negative charge separation to graupel was eliminated at higher temperatures ($T > -7.5$°C). A hybrid scheme (Fig. 1) was developed that merged the parameterization of Brooks et al. (1997) for temperature $T > -15$°C with Saunders and Peck (1998) for $T < -15$°C. Graupel collection efficiency for cloud droplets was set to a constant $E_{g,w} = 0.5$ for this study (Saunders et al. 1991). As in our previous studies, the effects of electric forces on dynamics are neglected.

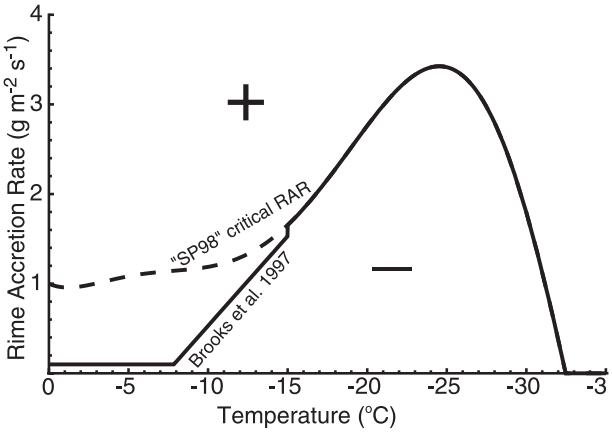

FIG. 1. Noninductive charge separation sign-reversal curve used in the present study. The critical rime accretion rate (RAR) curve follows Saunders and Peck (1998) for $T < -15$°C (shown as dashed curve for $T \geq -15$°C) and Brooks et al. (1997) at higher temperatures. Charge transfer is set to zero for $T < -33$°C.

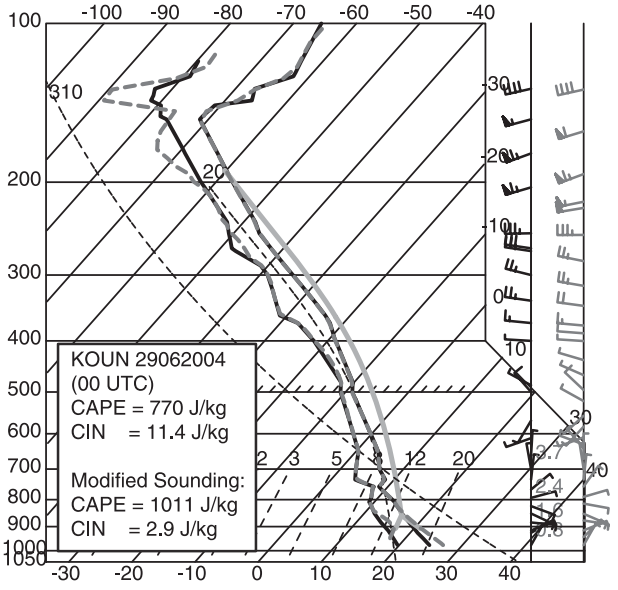

FIG. 2. Environmental sounding (solid curves) and model initialization sounding (dashed gray curves).

The model employs an updated version of the branched lightning parameterization of Mansell et al. (2002, 2005). Essentially the same lightning scheme has recently been employed by Riousset et al. (2007) and Krehbiel et al. (2008) with idealized time-dependent charge configurations (i.e., not in a microphysical storm model). Mansell et al. (2002) noted that a method was under testing to maintain charge neutrality of the channel structure by adjusting the electric potential of the channel similar to Mazur and Ruhnke (1998) instead of adjusting propagation thresholds, and this new method is now in use. The charge balance is checked after each lightning step, and if the channel ends are more than 2% out of balance, then the channel potential is shifted by the same amount all along its length until the imbalance is less than 2%. As in Mansell et al. (2002), a simple height threshold (here 500 m, or 4 grid points above ground) was used to declare a flash to be a CG (i.e., the flash was not required to propagate all the way to ground). Resistance is represented by an internal electric field, which in this study is set to 100 V m^{-1}. Another new feature is that the channel potentials are set to zero in the event of a CG flash, and further growth is allowed until the breakdown quenches itself.

Lightning initiation now uses the threshold for runaway air breakdown determined by Dwyer (2003) and scaled from standard air density as $E_{\text{init}} = 2.84 \times 10^5(\rho_{\text{air}}/\rho_0)$ V m^{-1}, which yields higher values than the relationship given by Marshall et al. (1995). The model presently does not take into account the depth over which electric fields exceed E_{init} (Dwyer 2003). The critical threshold electric field for channel propagation is still assumed to be some fraction of the initiation threshold, $E_{\text{crit}}(z) = f_{\text{crit}}E_{\text{init}}(z)$. The electric field (i.e., potential difference) between any given channel point and an adjacent point must exceed $E_{\text{crit}}(z)$ to have a nonzero probability of propagation to the adjacent point. To maintain similar lightning extents as the older, lower E_{init}, the present study uses $f_{\text{crit}} = 0.43$. The two-dimensional simulation study of Tan et al. (2006) found that lightning propagation was very sensitive to grid resolution, with much greater channel lengths achieved at 12.5-m resolution than at 250 m at the same propagation threshold. Thus the low value of f_{crit} is used here to compensate for inadequate resolution of the channels.

As described in Mansell et al. (2005), a ''potential domain'' is used for solving the Poisson equation that extends laterally and vertically beyond the dynamics domain to improve the solution within the dynamics domain, particularly at the top boundary. The boundary condition at the top of the potential domain now assumes a Dirichlet form $\phi = \phi_{z,\text{fw}}$, where the average fair weather (fw) electric potential $\phi_{z,\text{fw}}$ is found by numerical integration of the fair weather electric field (Gish 1944; Helsdon and Farley 1987).

3. Model initialization

The horizontally homogeneous model environment was initialized from a 0000 UTC 29 June 1994 National Weather Service operational sounding (Fig. 2) launched from Norman, OK. Tests with the unmodified sounding resulted in convection that decayed too rapidly after

updraft forcing (below) was turned off. Surface mesonet stations closer to the storm suggested the existence of locally higher surface temperatures, so the mixed boundary layer of the sounding was modified to match the higher potential temperature in the surface layer. The boundary layer moisture and temperature profiles were adjusted to maintain slight stability in θ_V (virtual potential temperature), which prevents spurious overturning in the boundary layer. The sounding modifications reduced the mixed layer convective inhibition (CIN) from 11.4 to 2.9 J kg^{-1} and increased CAPE from about 770 to 1011 J kg^{-1}, resulting in longer-lived simulated storms. Simulations were performed in a 30 km $\times$ 30 km $\times$ 21.6 km domain with constant grid spacing of 250 m in the horizontal and 125 m in the vertical from the surface to 10 km, above which the grid spacing was stretched to a maximum of 500 m. Lightning was propagated on a grid refined to 125-m horizontal grid spacing (with interpolated net charge density) to avoid propagation bias that can arise from unequal horizontal and vertical spacing. The model time step was 4 s.

Convection was initiated by a boundary layer updraft forcing term that was applied for the first 30 min of simulation. The cell of interest did not appear until about 60 min, which is well past the end of the forcing period. The forcing term imposed a maximum vertical acceleration of 1.75 $\times$ 10^{-2} m s^{-2} at the center of a spheroidal region in the center of the domain (horizontal radii of 8 km and vertical radius of 1 km, vertically centered at 1 km), dropping smoothly to zero at the edges as the square of the cosine function (as is typical for thermal bubble perturbations). The forcing turns off automatically at points where downward vertical motions exceed -0.1 m s^{-1} to allow downdrafts to exist in the forcing region (e.g., allowing horizontal roll circulations to form). Randomized thermal perturbations (maximum magnitude of 0.1 K) were applied in a larger region to simulate natural fluctuations. The model domain was translated roughly southwestward, with a motion vector of (-1.4, -0.5) m s^{-1}.

Considering the aforementioned observational inference by Bruning et al. (2007) from dual-polarization radar data that the warm-rain process was very active in this case, simulation tests were performed to determine an appropriate bulk CCN concentration that would promote sufficiently large cloud droplets to maintain an efficient collision–coalescence process. For this case, CCN concentrations were set at 350(ρ_{air}/ρ_0) cm^{-3}, where ρ_{air} is air density and ρ_0 = 1.225 kg m^{-3}. The model initiation of CCN concentration assumes that CCN are well mixed in the environment and scales the base CCN concentration by air density.

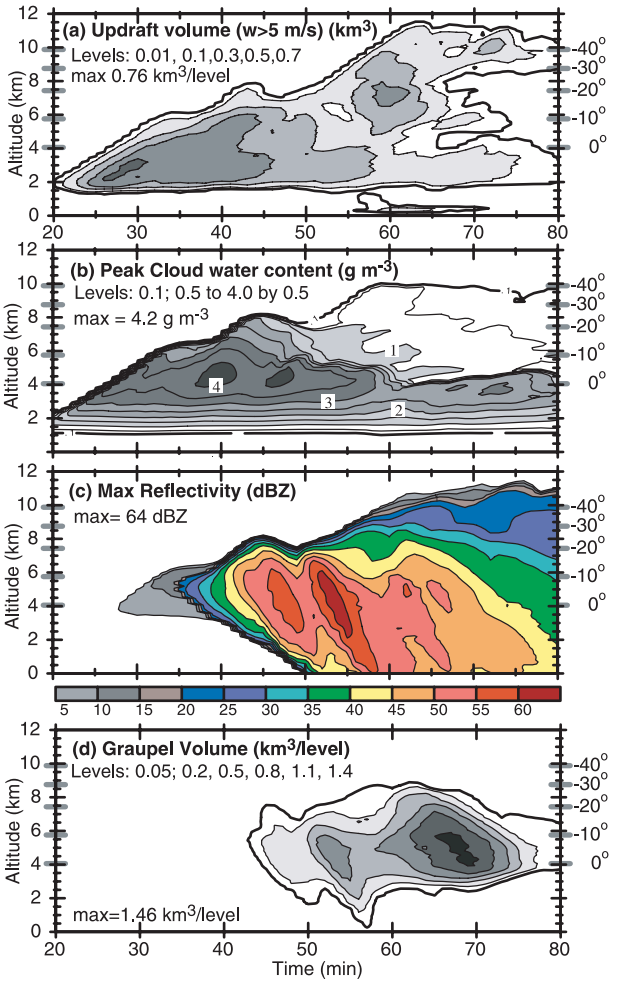

FIG. 3. Time–height quantities: (a) updraft volume per model level (125 m thickness), (b) maximum cloud water content, (c) maximum reflectivity, and (d) graupel volume per model level. Labels on the right-hand axis indicate environmental air temperature (also denoted by gray ticks on both axes).

4. Results

a. General microphysical evolution

Modeled precipitation initiated as raindrops via stochastic collision–coalescence in regions of high cloud water content just below the freezing level, resulting in the first reflectivity (Fig. 3c). Raindrops lifted in updrafts began freezing at temperatures around -10°C to form graupel. The time–height reflectivity (Fig. 3c) and graupel volume (Fig. 3d) show three maxima at about 45, 55, and 65 min, each preceded by a pulse in updraft volume (Fig. 3a). Peak cloud water contents (Fig. 3b) decreased significantly due to riming collection in the second and third reflectivity maxima as graupel volumes increased. Peak updraft (not shown) reached a maximum of 19.5 m s^{-1} at 40 min, later dropping to 10.2–12.1 m s^{-1} during the

significant electrical period of 60–74 min. After 74 min, peak updraft fell steadily to 6 m s^{-1} by 82 min, where it remained for the rest of the simulation (85 min).

The third storm pulse was distinguished from the previous ones by growth in height of the 30- dBZ height from about −20° to −30°C, the development of updraft above 6 km, and substantial increase in graupel volume, resulting in electrification sufficient for lightning (10 flashes over 11 min). Upward ice crystal flux through the −10°C isotherm (not shown) also increased dramatically from 55 to 60 min. Some ice crystals initiated from vapor deposition on ice nuclei, and these crystals helped initiate freezing of supercooled raindrops. A larger number of ice particles was produced by rime splintering (Hallett–Mossop process) in the temperature range of −8° to −3°C, and ice splinters were also produced by freezing drops at a chosen rate of one splinter per drop.

b. General electrical evolution

In the first and second reflectivity cores, graupel gained mostly positive charge from rebounding collisions with ice crystals in the temperature range of −5° to −15°C (Fig. 4a, 45–55 min) or roughly 5–6-km altitude. The positively charged graupel had much greater fall speed than the negatively charged small ice particles, whose charge remained much more concentrated and is evident at about 5 km in Fig. 4c. Charge separation was appreciable but insufficient for lightning, with peak electric fields magnitudes remaining below 50 kV m^{-1}.

Positive noninductive charging of graupel increased again at lower levels (5–7 km, −5° to −15°C) from 55 to 65 min (Fig. 4a). At the same time, graupel charged negatively at higher altitudes (6–9 km), where temperatures and rime accretion rates were lower. This combination of lower positive and upper negative charge separation resulted in three main charge regions by height, evident in the time–height net charge (Fig. 4d): lower positive charge at 4–5 km (graupel), main negative charge at 5–7 km (ice crystals and graupel), and upper positive charge at 7–9 km (ice crystals and snow). Negative charge at higher altitudes (8–10 km in Figs. 4c,d) is primarily in screening layers, which form from ion attachment to small cloud particles at cloud boundaries. The lower positive region in Fig. 4b was attached to faster-falling graupel and spread out vertically, and showed up as a clear peak only when the charge separation rates are higher (Fig. 4a).

Inductive charge separation between graupel and small droplets was allowed, but integrated rates were always at least an order of magnitude smaller than noninductive charging and therefore are not shown. The effects of inductive charge separation are weaker than seen by Mansell et al. (2005) because the two-moment

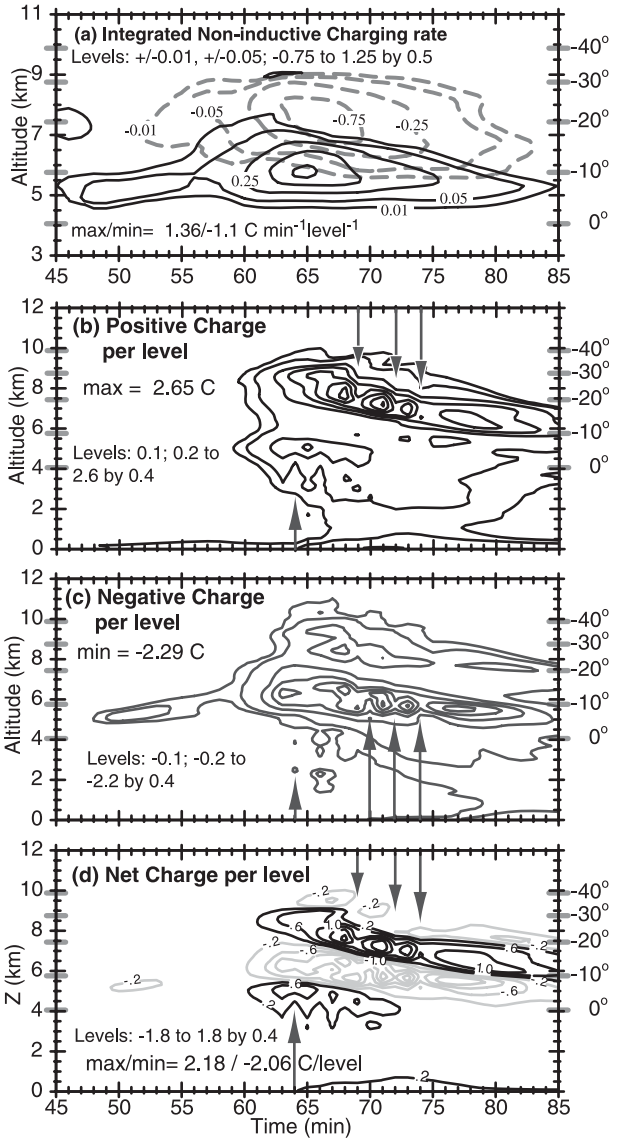

FIG. 4. (a) Noninductive charge separation rates, integrated by model level (125 m thickness), between graupel and ice crystals–snow. Polarity indicates the sign of charge gained by graupel. (b) Layer total positive charge. (c) Layer total negative charge. (d) Layer net charge. Arrows in (b)–(d) indicate the first lightning flash just before 64 min and lightning events with obvious effects on the layer charge.

scheme properly accounts for depletion of droplet concentration, whereas the single-moment scheme assumed a constant droplet concentration. In the single-moment scheme, a loss of droplet mass reduced droplet size, but not concentration, until the minimum allowed droplet size of 5 μm was reached.

In the first five minutes of simulated lightning activity, six flashes initiated between the main negative and lower positive charge regions, two −CG flashes and four

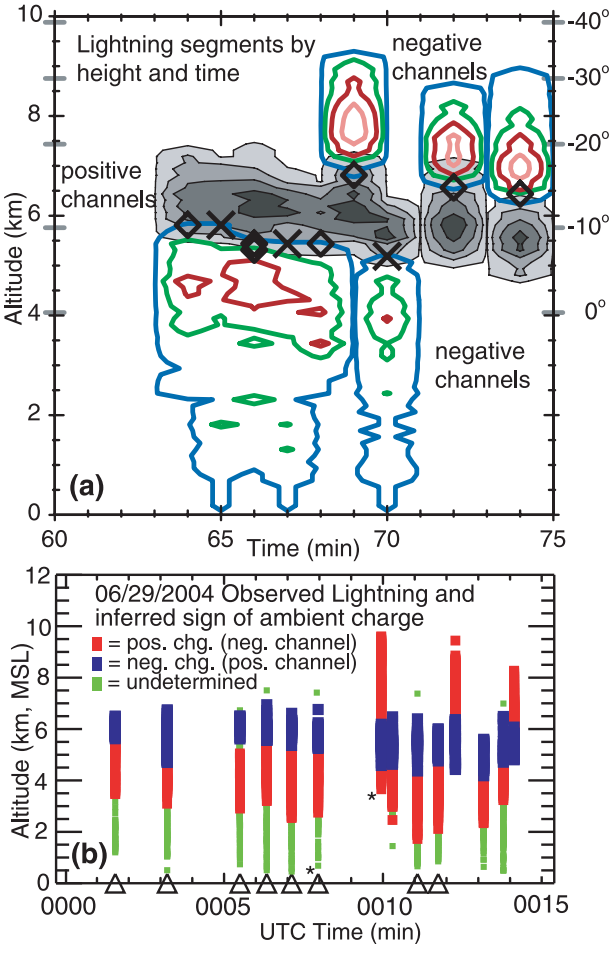

FIG. 5. (a) Time–height lightning channel segments per model level (negative: colored contours; positive: gray-filled contours). Contour levels are 0.75, 10, 25, and 50 segments per level. Initiation heights are indicated by diamonds (IC) and crosses (−CG). (b) Detected lightning sources from the first 14 flashes of the observed storm, colored by inferred ambient charge: negative (blue), positive (red), or undetermined (green). The triangles on the bottom axis denote flashes classified by the NLDN as −CG flashes. The sources from the two observed flashes denoted by an asterisk are displayed in Fig. 8d.

IC flashes (Fig. 5a; Table 1), compared with six −CG flashes in the first eight minutes of the observed case (Fig. 5b), which includes reports of −CG flashes from the National Lightning Detection Network (NLDN). The upper positive charge first became involved in lightning with the seventh flash (68:12) and then again with the final (IC) flashes, in a similar evolution as the observed storm. The effects of the three simulated upper IC flashes on the net positive charge are noted in Fig. 4b by arrows, which point to the sharp reductions in net positive charge. As would be expected from basic physics and the assumption of highly conductive, connected channels (Kasemir 1960), the heights of the positively and negatively charged lightning channel segments (Fig. 5a) correlate very well with the average heights of the charge layers (Fig. 4d, 65–70 min). More specifically, the correlation is with the maxima and minima in electric potential (e.g., MacGorman et al. 1981, 2001; Coleman et al. 2003), which are generally offset from the charge extrema.

c. *Lightning sensitivity*

Lightning activity from two sensitivity tests is shown in Fig. 6. In the first test, the critical propagation threshold factor f_{crit} was reduced to see if the first flash could become −CG rather than IC. A reduction from 0.43 to 0.40 was sufficient to achieve a −CG flash, but three of the six lower flashes still did not reach ground. Otherwise, the lightning was quite similar to the control run: 10 total, 3 −CG, 3 lower IC, and 4 upper IC flashes.

The second sensitivity test (Fig. 6b) shows results using the unmodified Saunders and Peck (1998) charge separation curve (Fig. 1). The reduction in positive charge transfer to graupel at lower altitude (higher temperature), or even reversal to negative charge transfer, results in only one −CG flash and two lower IC flashes. Three upper IC flashes were produced, as the control run did.

d. *Charge and reflectivity structure and lightning*

The evolution of charge and potential from just before the first flash to just after the second flash is represented at 20-s intervals in Fig. 7. The preflash structure (Fig. 7a) had three main charge regions, with the upper positive charge being the weakest. This structure might be described as a ''bottom-heavy'' tripole charge structure, in contrast to the conventional tripole model of strong upper positive charge and much smaller lower positive charge region. The first flash makes substantial reductions in the maximum positive and negative charge densities and in the maximum negative potential (Fig. 7b). Maximum positive potential was only slightly affected because the upper positive charge was not involved and maintained its potential, although the lower positive maximum was virtually eliminated (at least in the plane). Over the next minute (Figs. 7c,d), charge and potential maxima increased again until the −CG flash at 64:20 (Fig. 7e), which completely eliminated the negative potential region in the plane shown. Negative potentials quickly regenerated, however, just 20 s later (Fig. 7f).

The growth in strength of the upper positive charge region is evident in comparing the first and last panels of Fig. 7. In Fig. 7a, the main upper positive charge was in a small region on the right-hand side of the structure (X = 20–23 km), where the thin layer of positive charge at the left edge (X = 17 km) is a screening layer resulting from positive ions attaching to hydrometeors at the cloud

TABLE 1. Individual simulated discharge characteristics. For −CG flashes, the channel potential ϕ_{ref} is the value just before contact with ground, at which point ϕ_{ref} is reset to ground potential (zero). The P is the magnitude of the IC flash dipole moment vector with the sign of the vertical component, P_z. Here, $P < 0$ indicates "normal" polarity, and in this case $|P_z/P| > 0.84$. Charge transfer is the net charge transferred to the storm by CG flashes, or the amount of charge (in parentheses) deposited by the positive channels of IC flashes. Altitude for IC flashes is the height of the midpoint between the positive and negative charge centers, and for CG flashes it is the height of the monopole charge center.

Time (min:sec)	Flash Type	Initial ϕ_{ref} (MV)	Final ϕ_{ref} (MV)	$\Delta\phi_{ref}$ (MV)	Dipole Moment P (C km)	Charge Transfer (C)	Altitude (km)	Change in Electrical Energy (%)
63:20	IC	−42.9	−14.6	28.3	20.7	(10.0)	5.4	−74.2
64:20	−CG	−55.1	−20.2	34.9		10.4	6.5	−49.6
65:04	IC	−6.6	−4.7	1.8	12.2	(6.6)	5.4	−45.3
65:44	IC	−26.0	−14.9	11.1	17.6	(7.2)	5.0	−38.3
66:32	−CG	−45.6	−22.5	23.0		13.4	6.0	−29.0
67:28	IC	−31.0	−8.6	22.3	17.6	(8.0)	5.1	−33.5
68:12	IC	−21.3	1.2	22.5	−29.8	(15.5)	7.1	−79.4
69:40	−CG	−52.3	−19.5	32.8		10.3	6.3	−44.5
71:04	IC	14.5	3.5	−11.1	−21.5	(13.5)	6.6	−76.5
73:48	IC	−16.1	−4.0	12.1	−21.5	(11.7)	6.4	−79.8

boundary. Negative screening layers are also found above and to the lower right side of the stronger upper positive charge. Less than two minutes later (Fig. 7f), the maximum potential contour in upper positive charge grew from 15 to 45 MV. The negative screening layers also grew thicker and began to extend farther to the west (X = 18–20 km), where the upper positive charge also increased.

Simulated radar reflectivities near the times of three lightning flashes are shown in Fig. 8 along with a comparison radar cross section (with two observed flashes) of the observed storm. The vertical cross section of observed reflectivity was synthesized from gridded sweep data as in Bruning et al. (2007). Note that to capture the higher echo tops, the simulated reflectivity slices are taken 250–500 m north of the planes in Figs. 7, 9, indicated by the y value of the origin O(x, y) noted on each panel. Both the simulated and observed reflectivity patterns slope upward from west to east (left to right) as a consequence of stronger winds above the −20° level, reflected in the sloping upper positive charge layer and observed lightning. At 64:20, two reflectivity maxima are seen at X = 16 km and X = 19–20 km, with lightning initiating in the rightmost reflectivity (Fig. 8a). The two

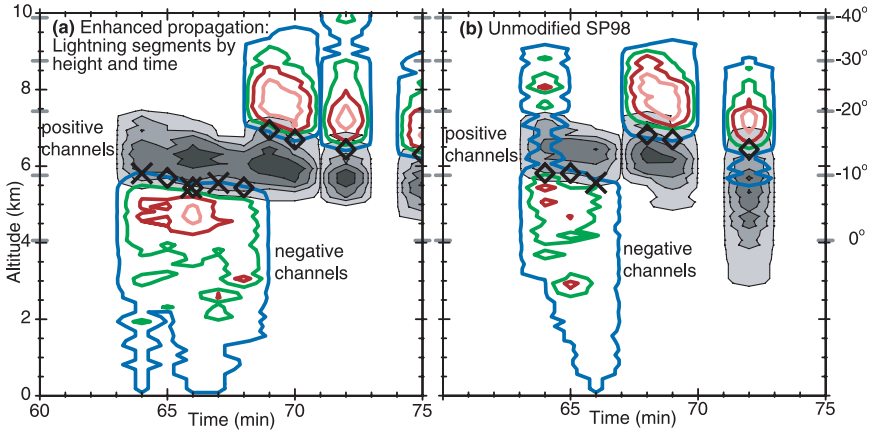

FIG. 6. Same as Fig. 5a, but (a) with the propagation threshold factor reduced from 0.43 to 0.40, which results in the first flash reaching ground, or (b) using the unmodified charge reversal curve (Fig. 1). The IC flash at 72 min in (a) propagated up into a cloud turret that was not accessed under the higher propagation threshold. The first IC flash in (b) at 64 min had a negative branch that propagated northwestward and upward into clear air. Contour levels are 0.75, 10, 25, and 50 segments per level (negative channels: colored contours; positive: gray-filled contours).

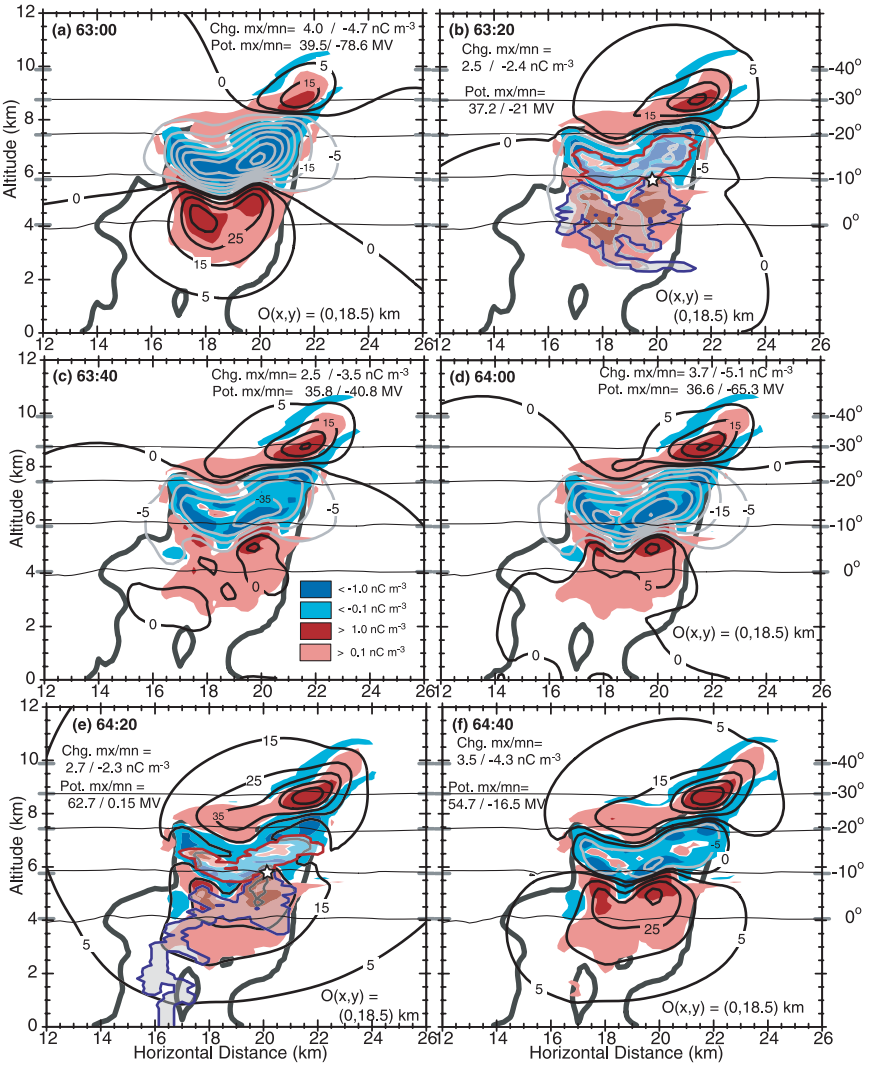

FIG. 7. Charge structure (color fill), electric potential (solid gray–black contours), and lightning projection (positive channels in red outline, negative in blue, both with transparent gray shading) at 20-s intervals. The wide dark curve is the 30-dBZ reflectivity contour. Hairline contours indicate air temperature (−30° to 0° by 10°C). (a) Structure 20 s before the first lightning flash [(b): white star at initiation point]. (e) The first −CG flash (second lightning) of the simulation. The origin point of the slice relative to the model domain is given by O(x, y), and horizontal distance is along a line at −16.7° from the true x axis.

regions of higher positive charge in the lower positive charge region (Fig. 7d) correspond to the two regions of updraft at X = 17 km and X = 19.5 km, just below the −10°C isotherm. The region of 45 dBZ at X = 17 km (5–6-km altitude) developed over the previous minute between the decaying left core and growing right-hand-side core. Lightning channels from the flashes at 63:20 and 64:20 (Figs. 7b,e) penetrated this region, which had substantial charge. Later, at 71:00 (Fig. 8b), the middle region had continued to grow and became the source of initiation of the upper IC flashes (Figs. 9b,c), with channels propagating back into the rightmost cell.

In the observed storm, Bruning et al. (2007) also noted lightning from one cell propagating into a new cell, in which lightning later initiated. Figure 8c shows the last flash of the storm, at which time the higher reflectivities (>40 dBZ) had fallen below the freezing level. The last flash at 74:00 also penetrated westward into the newer weak cell, whose charge at an earlier time can be seen in Fig. 9d. Lightning never initiated in this far western simulated cell.

At the mature stage of 69:20 min, the lower positive charge region (Fig. 10a) consisted mostly of positively charged graupel (Fig. 10c). The lower part of the main negative charge region also had positive graupel particles

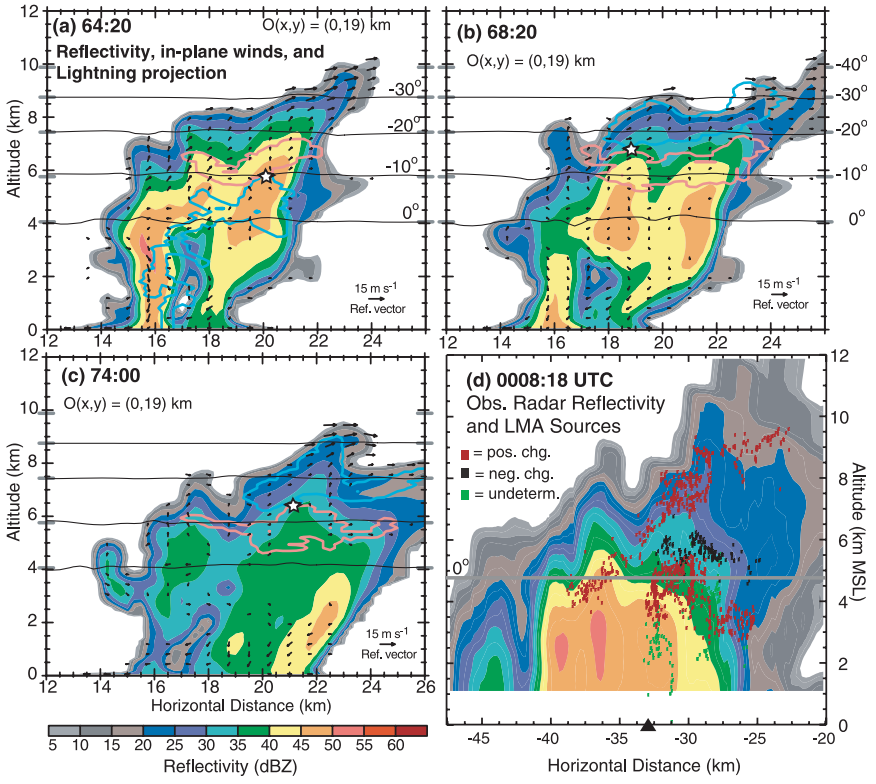

FIG. 8. Reflectivity and winds in a representative plane that is 500 m north of the plane used in Fig. 7. Lightning flash outlines and initiation points (white stars) are projected into the plane: positive channels (red outline), negative channels (blue outline), initiation points (white-filled area with black outline). Isotherms are represented by thin black contours. (a) First −CG flash (second flash overall, Fig. 7e). (b) First of the three upper IC flashes. (c) Last of the three upper IC flashes. (d) Observed radar reflectivity cross section at 103° with detected lightning sources from two lightning flashes (noted by the asterisks in Fig. 5b).

but more negative charge on small ice crystals and snow (Fig. 10d). The upper parts of the main negative region held negatively charged graupel, cloud ice and snow, along with positively charged cloud droplets and drizzle-sized raindrops (~200 μm diameter; Fig. 10e), which gained charge primarily from attachment of lightning-produced ions. (Raindrops may also be charged if they form by coalescence of charged cloud droplets.) A large fraction of ice crystals rising into the upper part of the negative charge region (about −12° to −17°C) grew sufficiently by vapor deposition to be converted into snow particles, which carried most of the charge in the upper positive charge region. Negatively charged graupel also existed in the upper positive charge region. Some portions of the thick negative screening layers at the top of the storm actually extended above the cloud boundary by up to 250 m (two grid points) as free ion charge (Fig. 10f), suggesting that significant small ion charge densities (>0.1 nC m^{-3}) may exist at the cloud exterior.

e. Electric field, energy, and net charge evolution

The maximum electric field showed essentially linear growth between 60 min and the first lightning flash (Fig. 11a), although the initial energy growth had increasing slope. The total electric energy appears to reach a maximum around 68 min, 2 minutes after a strong peak in graupel volume and 1 minute before a shallow maximum in updraft speed. The graupel volume, if shifted by 2–3 min, follows the trend in electrical energy quite well. Maximum updraft follows the decay trend but was decreasing during the initial growth in electric field and energy.

Each simulated flash reduced the total electrical energy by a substantial fraction (listed in Table 1), from 33% to almost 80%, followed by linear recovery in maximum electric field. The electric field and energy recovered somewhat even after the last simulated lightning flash (at 73:48; Fig. 11a), but it was insufficient to initiate lightning before charge separation ceased to be

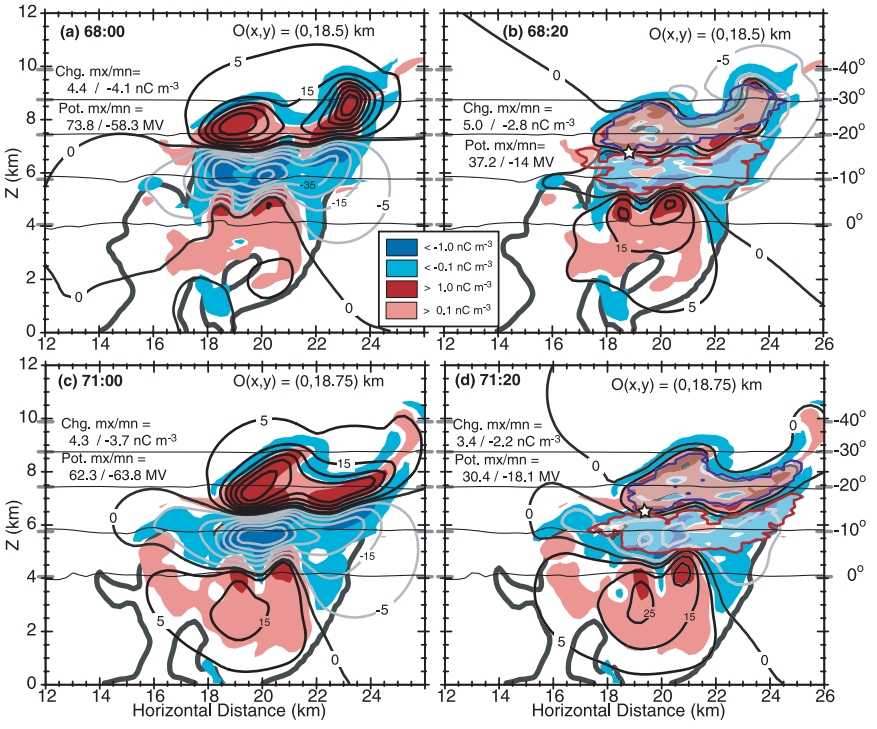

FIG. 9. Same as Fig. 7, but for first [(a),(b)] and last [(c),(d)] of the three upper IC discharges. Charge structure (color fill), electric potential (black–gray solid contours), lightning projection (positive channels in red outline; negative in blue), and 30-dBZ outline (wide dark curve). White stars indicate lightning initiation points.

greater than nonlightning dissipation processes. For comparison, the total gravitational energy of graupel at 65 min was 2.2×10^{12} J, about three orders of magnitude greater than the electrical energy. (This does not necessarily imply, however, that locally the electric force magnitude on a particle could not be an appreciable fraction of the gravitational force in regions of large electric fields.)

The electric field recovery after most flashes tended to have an initial slow linear growth followed abruptly by faster linear growth (Fig. 11a). This behavior is a result of continued diffusion of ions deposited by lightning, particularly when the ions are released in regions with fewer small hydrometeors, such as in the lower positive charge region. Small ions become attached to hydrometeors more quickly when many small particles are present, but they attach at lower rates to larger hydrometeors. Helsdon et al. (1992) noted in their model simulations that lightning ions in cloudy regions had mostly attached to hydrometeors within 2 s, whereas in precipitation regions with low concentrations of small hydrometeors, the density of lightning ions could remain significant for 30 s or more. They also noted continued reduction in charge on snow particles and on electric field for their intermediate (L3) flash case (Helsdon et al. 1992, their Figs. 6, 8) due to diffusion of lightning-produced ions. The storm simulated by Helsdon et al. (1992) assumed a high CCN concentration and thus high cloud droplet concentrations. In the present case, the cloud droplet concentrations are much lower as a result of lower CCN concentrations and scavenging by graupel, so that droplet concentrations in the main negative charge region were typically as low as 10–30 cm^{-3}, which decreased the rate of ion attachment. Helsdon et al. (1992) used single-moment microphysics, so droplet concentrations were much less affected by scavenging, keeping droplet concentrations and attachment rates higher than in the present two-moment model. Thus, longer lifetime for lightning ions deposited within the main negative charge region would be expected in the present simulation than was seen in Helsdon et al. (1992). The plot of maximum electric field magnitude in Fig. 11a suggests that lightning ions can affect the field recovery for up to 16–20 s (4–5 model time steps).

Figure 11a also plots the total electrical energy in the model domain, where a difference is seen in the response to IC and −CG flashes. The continued decrease in energy for a few time steps after −CG flashes appears to be a response in the ion flux into and out of the domain (Fig. 11b) to offset the sudden electric monopole

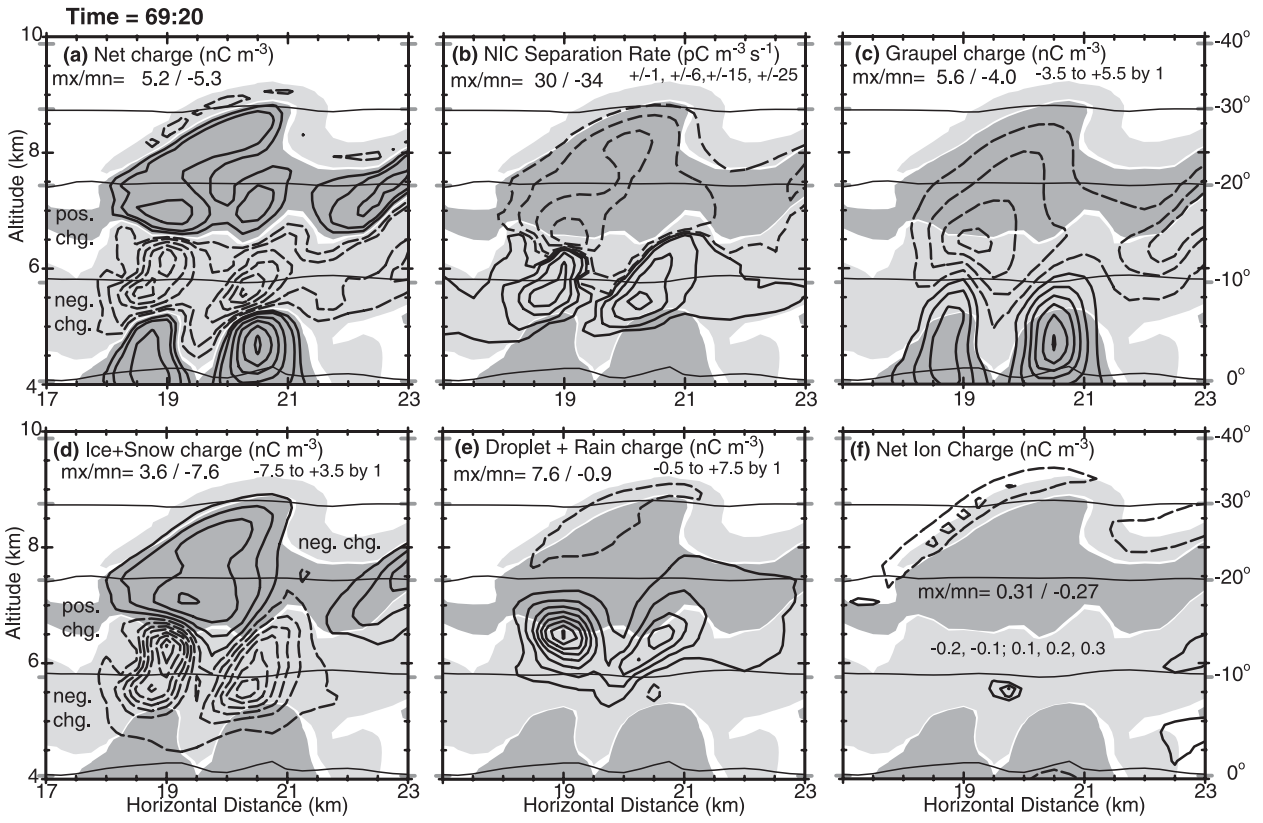

FIG. 10. Net charge, charging rates, and hydrometeor charges at 69:20 just before the last −CG flash. Positive contour lines are solid, negative lines are dashed. Background shading is for net positive charge (>0.1 nC m^{-3}, dark gray) and negative charge (<−0.1 nC m^{-3}, light gray). (a) Net charge, (b) noninductive charge (NIC) separation rate (graupel with ice and snow), (c) charge on graupel, (d) charge on ice crystals and snow, (e) charge on cloud droplets and rain, and (f) net free ion charge (note different scale on contours). Maximum and minimum values (mx/mn) are indicated on each panel.

moment change. The net ion flux is the total ion charge entering (or exiting) the domain via advection, ion drift, and corona discharge at the ground surface. The larger-scale ion currents acted to restore the net domain charge back toward preflash values, reducing the electric fields (and potentials) outside of the storm (e.g., compare the electric potentials in Figs. 7e,f).

The domain net charge remained positive throughout the life of the simulated storm until the final decay stage after the last lightning flash (Fig. 11b). Besides ion flux, net charge in the domain is affected by advection and sedimentation of charged hydrometeors out of the domain (or to the ground) and by CG lightning flashes. The net charge was most strongly affected by the −CG flashes, each of which brought substantial positive charge to the storm. The changes in total net positive charge were smaller than the changes in net charge because the positive charge from the −CG flash primarily masked negative charge (i.e., made the local net charge less negative). The total positive charge always showed some reduction after each flash (i.e., immediately following the circled points in Fig. 11b). This reduction was a result of continued drift of lightning ions (positive and negative) into surrounding regions of opposite charge.

The net domain ion flux responded sharply to all lightning flashes, with the monopole moments of the −CG flashes causing large spikes in ion flux that counteracted the change in net domain charge. The ion response to IC flashes was clearly dependent on the dipole moment, which mainly indicated that the model behaved as expected.

f. Simulated balloon sounding

A set of simulated instrumented balloon soundings were generated in the model, one of which is plotted in Fig. 12. The sounding was initiated at 59 min with an assumed rise rate of 10 m s^{-1} relative to vertical air motion. The simulated sounding resembled the observed electric field structure (vertical component, E_z; Bruning et al. 2007) quite well in terms of the sequence of the main positive and negative excursions, though generally the peaks were at higher altitudes than in the observed

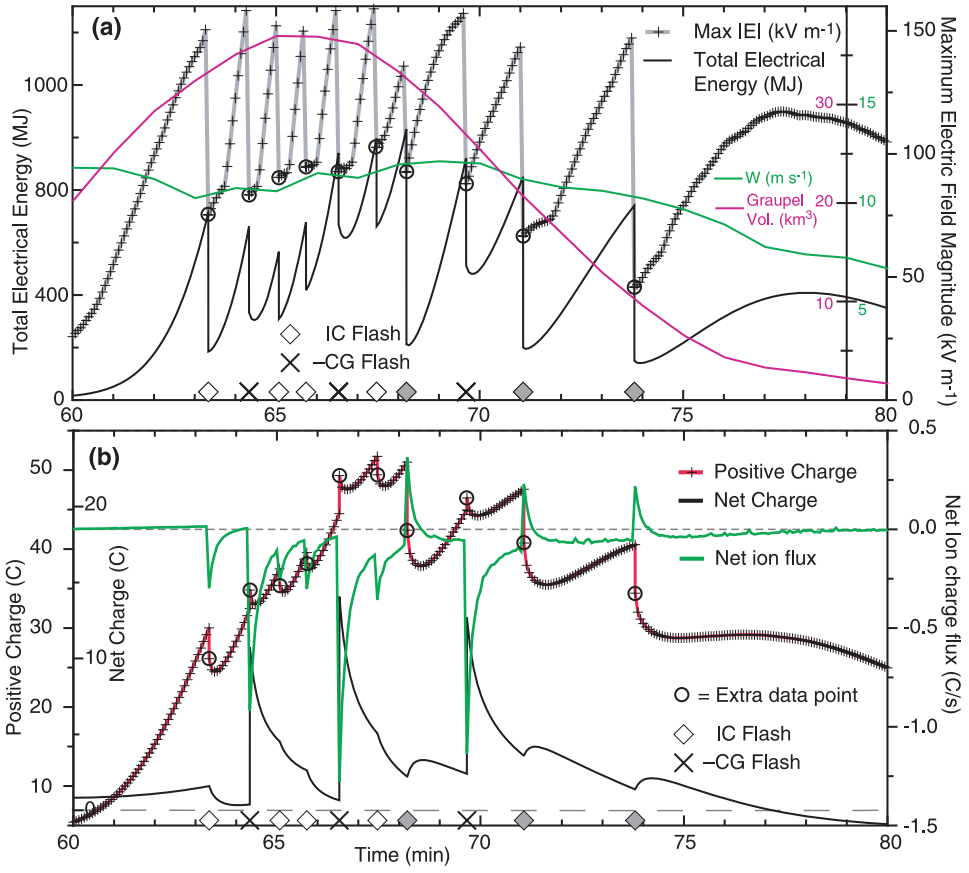

FIG. 11. Time evolution of (a) maximum electric field, total electrical energy, peak updraft (w), and graupel volume above the freezing level, and (b) net ion charge flux into the model domain and domain total net charge and positive charge. The time resolution is the model time step (4 s), and extra circled points denote values immediately following lightning flashes (excludes the effects of ion drift and attachment). The shaded IC flash symbols (diamond) indicate normal-polarity discharges (negative vertical dipole moment) between the main negative and upper positive charge regions.

sounding. Approximate peak values and AGL altitudes from the observed sounding are noted in Fig. 12 next to the simulated peaks at 5, 6.5, and 7.5 km. The simulated peaks are consistently at higher altitudes by 500–1300 m. The difference in altitudes could be simply a result of the modeled sounding occurring earlier in the storm life cycle when charge interfaces were higher. It is evident from Figs. 4b–d that the main charge regions descended with time. By about 80 min the charge interfaces between the main negative and upper positive and between the upper positive and negative screening layers (Fig. 4d) were closer in altitude to the upper two electric field peaks in the observed sounding.

The simulated sounding maintained water saturation from about 5.3 to 7.8 km, suggesting that the region sampled by the observed sounding, which showed subsaturation, was further into decay stage than for the same altitudes in the simulated sounding. The model did not produce any high relative humidities in the boundary layer that were indicated by the observed sounding. The model sounding also has a layer of cool storm outflow air in the lowest 300 m above the surface, but the observed sounding has no indication of storm outflow. The model presently has no surface physics (e.g., drag or heat and moisture fluxes) that might play roles in modifying downdraft air that reaches the surface.

5. Discussion

The observed TELEX storm (Bruning et al. 2007) produced a total of 30 lightning flashes over 38 min. Of these, 15 flashes were reported by the NLDN as −CG flashes. Lightning mapping array data analysis suggests that two more flashes were likely also negative −CG but missed by the NLDN. We judged three of the observed flashes between the main negative and lower positive charge regions to be IC flashes, based on LMA analysis and lack of detection by the NLDN. The remaining

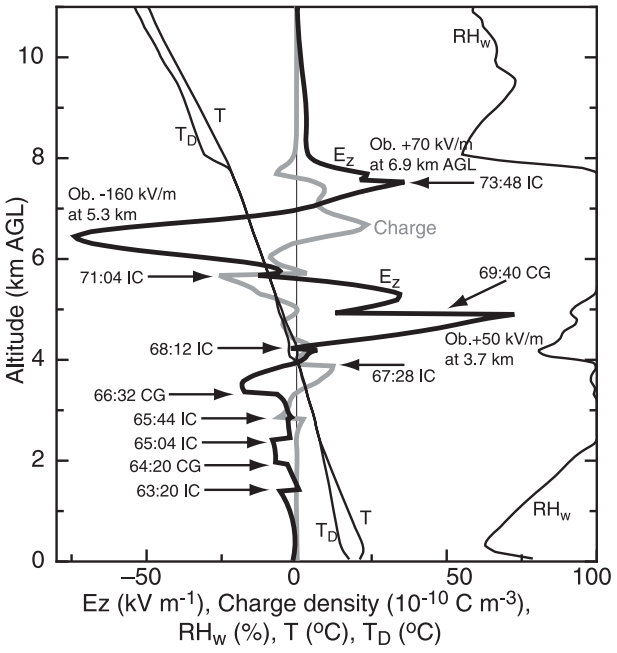

FIG. 12. Simulated balloon sounding profile of vertical electric field component E_z, net charge interpolated to the balloon location, air temperature T, dewpoint temperature T_D, and relative humidity (with respect to liquid water) RH_w. The simulated balloon trajectory assumed a rise rate of 10 m s^{-1} relative to the local vertical wind motion. The times and types of all 10 simulated flashes are indicated.

10 flashes were IC flashes involving the main negative and upper positive charge regions, with a few flashes also extending from the upper positive charge into the lower positive charge. The simulated storm had 10 flashes over 11 min for a comparable flash rate. The simulation also reproduced initial lightning in the lower charge regions followed by lightning in the upper charge regions. The ratio of upper to lower flashes in both the observed and simulated storms were both about 1:2, suggesting similar proportions of noninductive charge separation in the upper and lower regions of the storms. The fraction of lower IC flashes in the simulation (>50%), however, was much higher than in the observed storm and will be discussed further below.

a. Evolution of lightning activity

One of the notable features of the 28–29 June 2004 TELEX storm was that the first six lightning flashes were all −CG flashes, followed by additional IC flashes that involved an inferred upper positive charge region (Fig. 5b). The observed evolution suggested an initial charge structure (at first lighting) of at least a midlevel negative charge region and a lower positive region with a growing or developing upper positive charge region. Bruning et al. (2007) noted that although lightning did not indicate an upper positive charge before the seventh flash, this does not rule out the presence and influence of an upper positive region. In any event, the upper positive region would have needed some finite time to develop, but the observations provide no direct evidence of its growth.

If the charge structure at first lightning had equal charge magnitudes in the positive and negative regions, then the electric potential of the lightning channel ought to be close to zero and lack sufficient potential difference with the earth to propagate to ground. Thus the energetics would favor an IC flash rather than a −CG flash. The occurrence of −CG flashes, then, indicates a sufficient imbalance in the electric potentials of the positive and negative charge regions that the channel maintains a sufficiently negative potential to propagate to ground.

At least two mechanisms could reasonably be at work to cause an imbalance in the two charge regions: (i) the lower positive charge is reduced relative to the main negative by sedimentation of positively charged graupel and raindrops to the ground along with the upward flux and attachment of ions released by corona discharge, and (ii) charge separation in the upper part of the storm enhances the negative charge region while also creating an upper positive charge region. Assuming that each −CG flash removes most of the imbalance, the mechanisms at work must restore an imbalance before the next −CG flash. Both mechanisms are active in the model simulation, but at least in this case the effects of sedimentation and ion flux are much weaker than upper noninductive charge separation. The time scale for graupel and rain to fall more than 5 km to ground is on the order of 8 min, assuming an average fall speed of 10 m s^{-1}, also suggesting that although sedimentation is always acting, it would be a weaker effect and by itself may not be able to cause sufficient bias for CG lightning. Observed cases with exclusively IC lightning in a lower dipole (inferred negative over positive charge; Fig. 13a) at the beginning stages of a storm have also been described by Qie et al. (2005) using ground-level field-change data for a low-flash-rate storm on the Tibetan Plateau and by Wiens et al. (2005) using lightning mapping data for a higher-flash-rate storm.

Overall, the simulated storm and lightning were consistent with the observed flash behavior and with inferences based on those observations (charge structure in particular). The gross charge structure of the simulated storm before the first lightning had three major regions (Figs. 4d, 7a). The acquisition of positive charge by graupel in the lower part of the storm was more concentrated and intense than the negative charging in the upper part of the storm (Fig. 4a; 60–65 min), leading to higher charge densities and greater electric fields

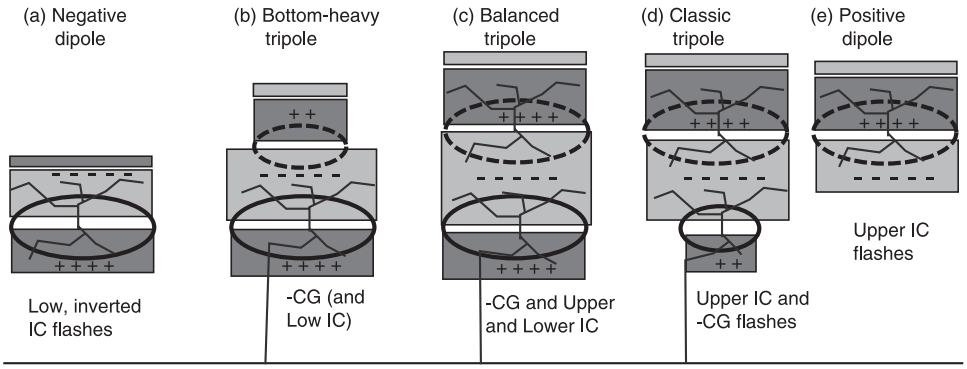

FIG. 13. Simplified models of charge structures and underlying noninductive charge separation. Solid ellipses denote graupel gaining positive charge, dashed ellipses indicate negative charging of graupel. Significant charge regions are noted by the shaded rectangles (light shading for net negative, darker shading for net positive charge). For inverted polarity storms, simply reverse all signs.

between the lower positive and midlevel negative regions. The first six lightning flashes in the model all initiated between the lower positive and midlevel negative charge regions, as in the observations. In contrast to the observed lightning, the simulation produced a mixture of −CG and IC flashes rather than all −CG, but the channel potentials all had a negative bias (Table 1, first six flashes). The negative charge separation (to graupel) at upper levels was thus responsible for enhancing the main negative charge relative to the lower positive charge and enabling −CG flashes.

The shortcomings of the lightning parameterization may be at least partially responsible for the discrepancy between the observed (CG only) and modeled (IC and CG) initial lightning flashes. A number of the observed −CG flashes either did not appear to connect immediately to ground from the initial negative leader breakdown or had subsequent breakdown activity more like IC lightning, as also observed by Coleman et al. (2008) for New Mexico storms. This suggests that the return stroke reduced the relative magnitude of the negative potential well, such that the subsequent breakdown no longer had sufficient bias to reach ground. The lightning parameterization, on the other hand, maintains a strong feedback between the positive and negative branches to maintain neutrality (before ground contact), and it assumes that channels always maintain high conductivity. The assumption of continuously highly conductive and connected channels throughout the discharge is certainly not the case in most lightning, as indicated, for example, by current cutoff and recoil leaders (e.g., Mazur 2002), where the channel is inferred to have cooled to lower conductivity and then is reionized to higher conductivity by the passage of a potential wave. The simulated −CG flashes therefore might overestimate the amount of positive charge brought up to the negative charge region, and thus could overly reduce the potential bias on the next flash so that it does not reach ground, as may have been the case in the observed storm for the first low IC flash. Note in Table 1 that the IC flash at 65:04 following the first CG flash had a much less negative channel potential (i.e., closer to zero), significantly reducing its likelihood of reaching ground. The first of the observed low, inverted IC flashes was the eighth flash of the storm (Fig. 5b). This observed flash occurred just after the first flash between the main negative and upper positive charge regions, which may have reduced the negative charge sufficiently to be more equal in magnitude to the lower positive charge.

b. Potential Well Hypothesis

The observed and simulated CG lightning behavior seems to be consistent with the data and "Potential Well Hypothesis" presented by Coleman et al. (2008). Coleman et al. (2008) found a relationship between the time interval from initiation to ground contact of −CG flashes in New Mexico storms and the extent of horizontal branching detected by the Langmuir Laboratory lightning mapping array: the delay time increased as the horizontal branching increased in the initial downward breakdown. This is consistent with a continuous range of relative magnitude of lower positive charge, proceeding from fast −CG flashes (little detected branching) and a very localized lower positive charge, through delayed −CG flashes with greater branching greater relative lower positive charge. Horizontal branching in −CG flashes then increases as the lower positive charge increases relative to the midlevel negative. At the end of the range, the positive charge would be sufficient to balance the main negative charge and constrain the discharges as intracloud, that is, prevent a −CG flash altogether. The ground-level vertical electric field values presented by Coleman et al.

(2008) are consistent with the relative magnitudes of the lower positive and main negative charges: "fast" −CG flashes occurred with positive electric field, suggesting dominance of the main negative charge, while slower −CG flashes occurred with less positive or negative field at the ground, suggesting a stronger lower positive charge relative to the main negative.

Coleman et al. (2008) interpreted the fastest −CG flashes as indicating the absence of a positive potential well, but an alternative explanation lies in the relative magnitude (and three-dimensional extents) of the positive to the negative potential regions or that the maximum potential in the positive charge region starts as a negative value. Indeed, Coleman et al. (2008) noted that most −CG return strokes were followed by more negative breakdown at the same altitudes as the first sequence of breakdown, from which ambient positive charge and a significant potential well would be inferred. The subsequent breakdown did not reach ground (IC-like flash behavior), however, which could be explained by action of the return stroke to deposit positive charge in the main negative charge region and shift the peak values of the negative and positive potential wells. (Consider, e.g., the positive shift in potential values at all levels between Figs. 7d,e.) The net positive charge brought up by the return stroke would cause the sharp negative change in electric field at the ground. In the actual extreme case of not even a relative maximum potential [e.g., the idealized charge structure in Mazur and Ruhnke (1998)], the positive charge region might be so localized that one would not expect any subsequent horizontal lightning activity.

Coleman et al. (2008) also noted positive ground-level electric field changes with some −CG flashes, particularly when the field was negative prior to the flash. The low, inverted IC flashes in the simulation also caused positive excursions in electric field at the ground (not shown) by bringing negative charge closer to ground, suggesting that those particular observed −CG flashes had the overall effect of an IC flash, that is, the change in net storm charge was small and the effect of the subsequent in-cloud discharge dominated over the charge deposited by the return stroke(s).

c. Net charge and CG flashes

The production of −CG flashes from the simulated storm that has net positive charge suggests that net negative storm charge is not a necessary condition. A hypothesis of Krehbiel (1986) [reiterated in Krehbiel et al. (2008)] was that a storm might acquire net negative charge in electrical screening layers via ion currents driven by a positive dipole storm charge structure. Net negative charge could then promote −CG flashes to drive the global electric circuit. Such a scenario may be feasible for a deep storm with a charge structure dominated by midlevel negative and upper-level positive charge (i.e., classic tripole). For the small storm simulated here, however, the sequence is the opposite: the −CG flash, driven by localized charge imbalance, causes a weakly positive storm to be much more positive, thereby driving negative ions toward the storm (Fig. 11b).

Wilson (1921) argued that the different mobilities of positive and negative atmospheric ions could lead to the negative potential region having greater magnitude than the positive region for either a positive or a negative dipole storm structure. If the negative region were consistently stronger, he thought, then lightning would tend to connect to the negative region more often than the positive. Wilson's argument did imply at least a slightly net negative storm charge, but it also rested on the relative magnitudes of the charge regions. In a broad sense, a significant net storm charge (positive or negative) might assist CG flashes of the same polarity by biasing the potential everywhere in the storm, and conversely it might retard opposite-polarity CG flashes. A sufficient local imbalance, on the other hand, can also promote CG lightning, despite the net storm charge. Thus, it might be possible for a net storm charge to be a contributing condition for CG flashes of the same polarity, but not necessary condition.

d. Charge descent

Bruning et al. (2007) estimated a 3 m s^{-1} rate of descent of the centroid of lightning breakdown sources in the upper charge layers of the observed storm (also noticeable in Fig. 5b in the uppermost sources) and a corresponding descent rate of distinctive features in the radar data. In the simulation, the interface between the upper positive and main negative charge regions descended from about 7 (Fig. 9a) to 6.5 km (Fig. 9c) in 3 min, or roughly 2.8 m s^{-1}, which agrees well. As noted above in section 4f, the time–height layer net charge (Fig. 4d) exhibits the reduction in average height of the charge layers, which also generally reflects the decreases in heights of peak positive and negative charging of graupel (Fig. 4a). The time–height lightning plot in Fig. 5 additionally shows that lightning initiation points fell in altitude with time. In Figs. 8b,c, the reflectivity contours generally descended with the charge layers and flash initiation heights, consistent with the observations (Bruning et al. 2007, their Fig. 8). Figure 10c shows a maximum negative graupel charge just below the main negative-upper positive charge interface, and this is generally true where graupel is gaining negative charge noninductively. In other words, the altitude of the negative-positive interface is driven by the altitude of maximum graupel

negative charging rate, which in turn depends on ice collision rate and impact speed, ambient temperature and rime accretion rate. In the simulated storm, those conditions are fairly well tracked by the 35-dBZ reflectivity top or by a graupel mixing ratio of about 0.8 g kg^{-1} (not shown).

Bruning et al. (2007) discussed the possible effect of small hydrometeors that collect ions from lightning discharges on the interface between the upper positive and main negative charge regions. This ''masking'' effect is seen to a degree in the model but is mainly associated with cloud droplets and small raindrops rather than with ice crystals. Lightning ions also attach to ice crystals and snow and reduce the charge they carry, but these particles can recharge via noninductive charge separation if they are in an active charging region. Figure 10e shows positively charged liquid drops that gained their charge by ion attachment and were then transported upward by updraft. The presence of the positive drops acts to bring the lower boundary of the upper positive charge downward by roughly 250–400 m at most. The effect is quite stable in time because the charged drops tend to be collected by graupel, limiting how far the drops can carry their charge. Thus, we find that some masking does occur but does not shift the boundary between net positive and negative charge over time.

e. *Field recovery after lightning*

The recovery of the maximum electric field and total electrical energy after a lightning flash is a combination of continued collisional charge separation coupled with differential sedimentation of oppositely charged particles. To examine the effect of differential sedimentation of preexisting charged particles alone, the model was restarted at 68:20, just after the first upper IC flash, with noninductive charge separation deactivated. The maximum electric field magnitude was 103 k V m^{-1} at the start and increased to a maximum value of 137 k V m^{-1} one minute later at 69:20, after which it oscillated slowly in the range of 126–139 k V m^{-1} until peaking again at roughly 71:00, when the total electrical energy also peaked. The electrical energy more than quadrupled from a starting value of 230 to 956 MJ. Despite the field and energy increases from differential sedimentation, however, no lightning was initiated. This result suggests that continued noninductive charge separation is needed for repeated lightning, at least for a small storm, such that any lightning activity would indicate ongoing noninductive charging.

6. Conclusions

The basic behavior of the 28–29 June 2004 multicell storm was quite well represented by the model simulation, whose results support some of the interpretations previously made from observations alone. The initial dominant negative-over-positive charge structure with a weaker upper positive charge (''bottom-heavy'' tripole, Fig. 13b) that later became more dominant (balanced tripole, Fig. 13c) was produced by noninductive charge separation between graupel and small ice particles. The classic tripole charge structure hypothesis (Fig. 13d) of a smaller lower positive charge region does not fit in this case, except perhaps in the decay stage of the storm. The bottom-heavy charge structure allows initial lightning activity between the main negative and lower positive charge regions while creating enough bias in the potential to produce −CG flashes. Both the model and the observed storm produced IC flashes between the lower two regions, suggesting that sufficient potential bias was not always present. The conclusions are consistent with observations of IC lightning in a lower dipole (e.g., Qie et al. 2005; Wiens et al. 2005) and the variation of time from initiation to return stroke in −CG lighting reported by Coleman et al. (2008).

Model results suggest that local charge and potential imbalance are a primary condition for CG lightning. Net storm charge may play an inhibiting role for CG flashes of opposite polarity, and it is not a necessary condition for CG flashes of the same polarity, although it may contribute by its effect on electric potentials within the storm.

Noninductive charge separation alone was found to be sufficient to produce strong charging at higher temperatures without much need for inductive graupel-droplet charge separation. Mansell et al. (2005) found this to be possible with the single-moment microphysics if higher ice concentrations were assumed. In the simulated storm, the vast majority of ice crystals at higher temperatures was produced by rime splintering and drop shattering, which require at least a two-moment microphysics scheme for prediction. Inductive graupel-droplet charge separation, on the other hand, was found to be less significant because of lower droplet concentrations resulting from low CCN concentrations, drop coalescence, and collection by larger particles.

Repeated initiation of lightning in a given region indicates active charge separation, at least for low-flash-rate storms. For higher-charge separation rates, it might be possible for differential sedimentation to restore the electric field sufficiently for a subsequent flash after charge separation has ceased, but it seems unlikely that lightning activity would continue very long after charging has stopped. When lightning is observed repeatedly in storm regions where updrafts are weak and little or no riming growth is expected (e.g., in anvils at temperatures $T < -40$°C where no liquid water should be present), other charging conditions might be considered,

such as supersaturation with respect to ice as a sufficient condition for appreciable charge separation (Mitzeva et al. 2006).

Acknowledgments. Support was provided by the National Severe Storms Laboratory and grants from the National Science Foundation (ATM-0119398 and ATM-0451639). Funding for this research also was provided under NOAA–University of Oklahoma Cooperative Agreement NA17RJ1227. We thank Louis Wicker, Donald MacGorman, and Jerry Straka for advice and discussions on numerical modeling, electrification, and microphysics. Anonymous reviews also helped to improve the manuscript. Special thanks to all those who assisted in data collection during the TELEX field program.

APPENDIX A

Microphysics

The microphysics scheme is an outgrowth and adaptation of Ziegler (1985) [extended in Zrnić et al. (1993)]. The concept of using rime mass density is applied from Straka and Mansell (2005) to provide greater diversity in fall speed of graupel and hail. A number of the equations from Ziegler (1985) will be repeated for easier reference, conversion of unit system from cgs to mks, and corrections.

Ziegler (1985) used bulk-size distributions that were functions of either particle volume, v, or diameter, D. To simplify interactions between categories with different distributions and to allow for greater flexibility in choosing shape parameters, we adapted the conventions of Seifert and Beheng (2006), who used a distribution function in terms of particle mass, but written here in terms of volume:

$$N(v) = A\frac{v^{\nu}}{\overline{v}^{\nu+1}}\exp\left[-B\left(\frac{v}{\overline{v}}\right)^{\mu}\right], \tag{A1}$$

$$A = \frac{\mu N_t}{\Gamma\left(\dfrac{\nu+1}{\mu}\right)}B^{(\nu+1)/\mu}, \tag{A2}$$

$$B = \left[\frac{\Gamma\left(\dfrac{\nu+1}{\mu}\right)}{\Gamma\left(\dfrac{\nu+2}{\mu}\right)}\right]^{-\mu}. \tag{A3}$$

Using the relationships

$$v = \frac{\pi}{6}D^3 \tag{A4}$$

TABLE A1. Hydrometeor species and relevant parameters. A range of particle densities indicates imposed limits when density is predicted.

Category	Abbreviation	ν	μ	α	Density (kg m^{-3})
Cloud Droplets	W	0	1	NA	1000
Rain	R	−0.8	1	NA	1000
Cloud Ice	CI	0	1	NA	900
Snow	S	−0.8	1	NA	100
Graupel	G	−2/3	1/3	0	300–900
Hail	H	−1/3	1/3	1	500–900

$$dv = \frac{\pi}{2}D^2\,dD, \tag{A5}$$

Eq. (A1) can be transformed into the more common dependence on diameter:

$$N(D) = 3A\frac{D^{3\nu+2}}{\overline{D}^{3\nu+3}}\exp\left[-B\left(\frac{D}{\overline{D}}\right)^{3\mu}\right] = 3A\frac{D^{\alpha}}{\overline{D}^{\alpha+1}}\exp\left[-B\left(\frac{D}{\overline{D}}\right)^{3\mu}\right], \tag{A6}$$

where $\alpha = 3\nu + 2$ [or $\nu = (\alpha - 2)/3$].

The hydrometeor classes and size distribution parameters are summarized in Table A1. The shape parameters (ν or α) for graupel and hail can be set at runtime, but the rest are currently nonadjustable. Graupel and hail particle densities can either be set as arbitrary constants or be predicted (as described below), for which the allowed range is given. The graupel category incorporates frozen drops, accounting for the upper limit of 900 kg m^{-3}.

a. Cloud droplet initiation and growth

The initiation of cloud droplets follows Ziegler (1985). For the first appearance of supersaturation at grid point, the mass of initiated droplets is calculated either by a one-step adjustment as in Klemp and Wilhelmson (1978a) or by an iterative saturation adjustment, and the number concentration initiated at cloud base is adapted from Twomey (1959):

$$C_{N,\mathrm{cb}} = \frac{1}{\Delta t}10^6(10^{-6}C)^{2/(k+2)}\left[\frac{1.63w^{3/2}}{kB(3/2,\,k/2)}\right]^{k/(k+2)}, \tag{A7}$$

where C is the assumed CCN concentration, k is the exponent in the relation $N_{\mathrm{CCN}} = CS_w^k$, w is the updraft speed, and B is the complete beta function. For the initiation rate C_N within the cloud, the vertical gradient of supersaturation in Ziegler (1985) is replaced with the full gradient [$w(\partial S/\partial z) \rightarrow \mathbf{V}\cdot\nabla S_w$]:

$$C_N = CkS_w^{k-1}\mathbf{V} \cdot \nabla S_w. \quad \text{(A8)}$$

Condensation can be a rapid process, particularly for smaller droplets. It was found that the linear growth equation in Ziegler (1985) could result in undersaturation in such conditions (i.e., overprediction of condensation). The single equation was therefore replaced with a Runge–Kutta integration across the time step, holding all conditions fixed except temperature and water vapor. Raindrops, if present, are included in the iteration.

We note here that Eqs. (A18) and (A20) in Ziegler (1985) were missing a factor of $3^{1/3}$, so that the coefficient should be $4\pi[3/(4\pi)]^{1/3}$, or 7.7955. Otherwise, rain evaporation is calculated as in Eq. (A20) of Ziegler (1985).

b. Autoconversion

Autoconversion is treated as in Ziegler (1985). The number concentration reduction in cloud droplets due to collision–coalescence is

$$\text{nccnc} = a_1 n_c^2 v_c^2 \frac{(\nu_c + 2)}{(\nu_c + 1)}, \quad \text{(A9)}$$

where n_c is cloud droplet number concentration, v_c is the mean droplet volume, and $a_1 = 9.44 \times 10^{15}$ m^{-3} s^{-1}.

The rate of mass (mixing ratio, q) conversion (cn) to rain (r) from droplets (w) is given by

$$\text{qrcnw} = \frac{L_2}{\rho_{\text{air}}\tau}. \quad \text{(A10)}$$

The number concentration rate of conversion is given by

$$\text{nrcnw} = \frac{3.5 \times 10^9 L_2}{\tau}. \quad \text{(A11)}$$

The variance-scaled droplet radius r_b is given by

$$r_b = \overline{R}_c(1 + \nu_c)^{-1/6}, \quad \text{(A12)}$$

where $\overline{R}_c$ is the mean volume droplet radius.

If $r_b > 7.5 \times 10^{-6}$ m, then the conversion time scale τ is

$$\tau = \frac{3.7 \times 10^{-6}}{(r_b - 7.5 \times 10^{-6})\rho_{\text{air}} q_c}, \quad \text{(A13)}$$

otherwise for $r_b \le 7.5 \times 10^{-6}$ m, no conversion takes place (Berry and Reinhardt 1974). The quantity L_2 is the mass content of drops converting from the small-droplet (cloud) to large-drop (rain) category (Berry and Reinhardt 1974):

$$L_2 = 2.7 \times 10^{-2}[(0.5 \times 10^{20} r_b^3 \overline{D}_c) - 0.4]\rho_c n_c v_c. \quad \text{(A14)}$$

c. Accretion

Raindrops can accrete cloud droplets when either the mean volume rain diameter $\overline{R}_r > r_H$ or the rain number concentration $n_r > n_H$, where the thresholds from Berry and Reinhardt (1974) are given by

$$r_H = \max\left[\overline{R}_c, \frac{6.3 \times 10^{-10}}{(r_b - 3.5 \times 10^{-6})}\right], \quad \text{(A15)}$$

$$n_H = f(3.5 \times 10^9 L_2), \quad \text{(A16)}$$

where $f = 1.2$ (Ziegler 1985) is a factor to allow sufficient time for the number of raindrops to exceed the number of drops in the large-drop spectrum when it first appears (Berry and Reinhardt 1974). The value of r_H is defined only when $r_b > 3.5 \times 10^{-6}$ m, otherwise $r_H = \infty$. (The subscript H denotes the ''hump'' of the large-drop spectrum.)

The rates of mass (q) gained by rain (r) by accretion (ac) of droplets (w) (qracw) and number concentration lost by droplets (nracw) are, for $\overline{R}_r > 50$ μm,

$$\text{nracw} = a_2 n_r n_c(\overline{v}_c + \overline{v}_r), \quad \text{(A17)}$$

$$\text{qracw} = \frac{a_2 n_r n_c \rho_c \overline{v}_c[(\nu_c + 2)\overline{v}_c/(\nu_c + 1) + \overline{v}_r]}{\rho_{\text{air}}}, \quad \text{(A18)}$$

and for $\overline{R}_r \le 50$ μm,

$$\text{nracw} = a_1 n_r n_c\left[\frac{(\nu_c + 2)\overline{v}_c^2}{(\nu_c + 1)} + \frac{(\nu_r + 2)\overline{v}_r^2}{(\nu_r + 1)}\right], \quad \text{(A19)}$$

$$\text{qracw} = a_1 n_r n_c \frac{\rho_c}{\rho_{\text{air}}}\left[\frac{(\nu_c + 3)(\nu_c + 2)\overline{v}_c^3}{(\nu_c + 1)^2} + \frac{(\nu_r + 2)\overline{v}_c\overline{v}_r^2}{(\nu_r + 1)}\right], \quad \text{(A20)}$$

where $a_2 = 5.78 \times 10^3$ s^{-1} (Long 1974).

d. Rain freezing

Probabilistic rain freezing (Bigg 1953) follows the Ziegler (1985) adaptation of the Wisner et al. (1972) parameterization:

$$\text{qrfrz} = \rho_r B' n_r \overline{v}_r^2 \frac{(\nu_r + 2)}{(\nu_r + 1)}[\exp(A' T_c) - 1], \quad \text{(A21)}$$

where T_c is the undercooling. Rather than attempting to partition the frozen drops into separate ice categories (e.g., snow, graupel, and hail), they are assumed to become graupel particles with density of 900 kg m^{-3} with a minimum mean diameter (default minimum diameter is 500×10^{-6} m) to prevent the mean graupel size from becoming too small, such that the process does not necessarily conserve particle concentration. Graupel particles can then serve as hail embryos.

Heterogeneous drop freezing can also be initiated by continuous collection and capture of ice crystals. Using the rain fall-speed function (A25), the rate of mass and number of freezing drops are given by

$$\begin{aligned}\text{niacr} = 0.2172[&0.2302\overline{D}_r^2 + 15823\overline{D}_r^3 \\ &- 4.168 \times 10^6\overline{D}_r^4 + 4.920 \times 10^8\overline{D}_r^5 \\ &- 2.133 \times 10^{10}\overline{D}_r^6]\, n_i\, n_r f_i\, f_r, \end{aligned} \tag{A22}$$

$$\begin{aligned}\text{qiacr} = \left(\frac{\rho_r}{\rho_{\text{air}}}\right)0.2172[&0.5223\overline{D}_r^5 + 49711\overline{D}_r^6 \\ &- 1.673 \times 10^7\overline{D}_r^7 + 2.404 \times 10^9\overline{D}_r^8 \\ &- 1.229 \times 10^{11}\overline{D}_r^9]\, n_i\, n_r f_i\, f_r, \end{aligned} \tag{A23}$$

where f_i and f_r are the fractions of crystals and drops with diameters greater than a specified minimum (in the present study, 10 μm for crystals and 500 μm for drops). The use of fractions here generally underpredicts the rate and mean size of drop freezing compared to an incomplete integration over drop size, but it has the benefit of avoiding numerical problems that can arise from generating small number concentrations of large graupel. The total amount of rain allowed to freeze (inhomogeneously or by ice capture) is limited by heat balance following the approach of Ferrier (1994).

e. Ice crystal initiation

Vapor nucleation of pristine ice crystals follows Ferrier (1994) and Meyers et al. (1992). Initiation at temperatures greater than −5°C can be enabled at runtime. Rime splintering (Hallett and Mossop 1974) is treated as in Ziegler et al. (1986). Contact freezing nucleation, which follows Cotton et al. (1986) and Meyers et al. (1992), is allowed, but it has been found to be very weak compared to primary vapor nucleation.

An option is included to produce small ice splinters from freezing drops, following Chisnell and Latham (1974), who argued that very small splinters would not be detected in experiments conducted in subsaturated air because they would quickly sublimate. They restricted the range of drop sizes to 50–1000 μm, but the parameterization here simply multiplies the number of frozen drops (by any mechanism) by the number of splinters per drop, N_{splint}. The default mass of the splinters is the minimum considered by the model, which corresponds to a 12-μm columnar ice crystal.

f. Terminal fall speed

All hydrometeor species have nonzero fall speeds, and, except for cloud droplets, have separate mass- and number-weighted average terminal speeds. In previous two-moment schemes (e.g., Ziegler 1985; Ferrier et al. 1995), number concentration fallout was calculated with the mass-weighted fall speed because of problems that can arise when mass falls faster than number concentration (Wacker and Seifert 2001; Milbrandt and Yau 2005a). Here, artifacts are controlled by substituting mass-weighted sedimentation of number concentration when an increase in reflectivity is detected.

Cloud droplet fall speed follows Straka and Mansell (2005):

$$V_{T,c} = \frac{g(\rho_w - \overline{\rho}_{\text{air}})\overline{D}_w^2}{18\overline{\rho}_{\text{air}}\nu_k} \approx \frac{g\rho_w\overline{D}_w^2}{18\overline{\rho}_{\text{air}}\nu_k}. \tag{A24}$$

Rain fall speed is calculated using a quartic polynomial fit to the data of Gunn and Kinzer (1949):

$$\begin{aligned}V_{T,r}(D) = 0.09112 &+ 4377D - 6.972 \times 10^5 D^2 \\ &+ 4.495 \times 10^7 D^3 - 9.835 \times 10^8 D^4. \end{aligned} \tag{A25}$$

The integrated mass-weighted (m) and number-weighted (n) are then

$$\begin{aligned}V_{T,r,m}(\overline{D}) = \gamma\frac{6}{\pi}(&0.04771 + 3788.0\overline{D} \\ &- 1.105 \times 10^6\overline{D}^2 + 1.412 \times 10^8\overline{D}^3 \\ &- 6.527 \times 10^9\overline{D}^4), \end{aligned} \tag{A26}$$

$$\begin{aligned}V_{T,r,n}(\overline{D}) = \gamma(&0.09112 + 2714.0\overline{D} \\ &- 4.872 \times 10^5\overline{D}^2 + 4.495 \times 10^7\overline{D}^3 \\ &- 1.626 \times 10^9\overline{D}^4). \end{aligned} \tag{A27}$$

Ice crystals are treated as columns, using mass–diameter and fall speed relations in Straka and Mansell (2005), which are transformed for dependence on particle volume:

$$V_{T,i}(v) = \gamma a_i v_i^{b_i}, \tag{A28}$$

$$V_{T,i,n}(\overline{v}) = \frac{a_i \Gamma(b_i + \nu_i + 1)}{(\nu_i + 1)^{b_i} \Gamma(\nu_i + 1)} \gamma \overline{v}^{b_i}, \quad \text{(A29)}$$

$$V_{T,i,m}(\overline{v}) = \frac{a_i \Gamma(b_i + \nu_i + 2)}{(\nu_i + 1)^{b_i} \Gamma(\nu_i + 2)} \gamma \overline{v}^{b_i}. \quad \text{(A30)}$$

Snow terminal fall speeds follow from Zrnić et al. (1993),

$$V_{T,s,m}(\overline{D}) = \frac{5.61743\,\Gamma(\nu_s + 25/12)}{\pi^{1/12}(\nu_s + 1)^{13/12}\Gamma(\nu_s + 1)} \gamma \overline{v}_s^{1/12}, \quad \text{(A31)}$$

$$V_{T,s,n}(\overline{D}) = \frac{5.61743\,\Gamma(\nu_s + 13/12)}{\pi^{1/12}(\nu_s + 1)^{1/12}\Gamma(\nu_s + 1)} \gamma \overline{v}_s^{1/12}, \quad \text{(A32)}$$

and when evaluated for $\nu_s = -0.8$ become

$$V_{T,s,m}(\overline{D}) = 5.72462 \gamma \overline{v}^{(1/12)}. \quad \text{(A33)}$$

$$V_{T,s,n}(\overline{D}) = 4.04091 \gamma \overline{v}^{(1/12)}. \quad \text{(A34)}$$

Graupel fall speeds are determined by the formulation of Wisner et al. (1972) and otherwise follow Ferrier (1994):

$$V_{T,g}(D) = \gamma a_g D^{b_g}, \quad \text{(A35)}$$

where

$$a_g = \left(\frac{4\rho_g g}{3 C_D \rho_{\text{air}}}\right)^{1/2}, \quad \text{(A36)}$$

$$b_g = \frac{1}{2}. \quad \text{(A37)}$$

The drag coefficient C_D can be set either to a constant or to a value scaled by particle density. For graupel the constant value is 0.8, and the linearly scaled value is in the range 0.45–0.8 for particle densities of $\rho_g = 800-500$ kg m^{-3} (i.e., lower C_D for higher ρ_g). The dependence on both density and drag coefficient encompasses the range of fall speeds of the four single-moment graupel categories in Straka and Mansell (2005) (low-, medium-, and high-density graupel, and frozen drops) within a single two-moment graupel category. Hail fall speed is treated the same as graupel, except that the range of C_D values is 0.45–0.6. The default range of C_D can also be changed to user-selected values at runtime.

g. Graupel bulk density

Farley (1987) showed that in a spectral microphysics scheme, variable graupel density could have significant effects on growth rate and residence time. Little to no numerical modeling since then has tried to incorporate prediction of graupel density in bulk microphysics. One problem with the implementation in Farley (1987) is that particle density was treated as the state variable. As an intensive variable, particle density is subject to substantial errors in advection and turbulent mixing. An appropriate solution is to use integrated particle volume content $\tilde{v}$ as the predicted variable, such that $\rho_g = \rho_{\text{air}} q_g / \tilde{v}$. The particle volume can be treated exactly like mixing ratio q except that it must be scaled by air density to account for compressibility. Thus, the actual advection variable is $(\tilde{v}/\rho_{\text{air}})$, or integrated particle volume mixing ratio.

The average density of rime accreted by ice species x follows Rasmussen and Heymsfield (1985):

$$\rho_{x,\text{rime}} = c_{\text{r1}} \left[\frac{0.5 \times 10^6 D_w (0.6 |\overline{V}_{T,x,m} - V_w|)}{-(T - T_0)}\right]^{c_{\text{r2}}}. \quad \text{(A38)}$$

For graupel, the average rime density was initially computed by a numerical integration over the graupel size distribution, but it was found that the bulk formulation performed very well in comparison. The volume of rime added to graupel (or hail) is simply $\tilde{v}_{\text{rime}} = \rho_{\text{air}} q_{\text{rime}} / \rho_{x,\text{rime}}$. When graupel or hail collects raindrops in dry growth mode, the drops are assumed to add ice volume at a density of 900 kg m^{-3}. In wet growth mode, the frozen portion of collected supercooled water (cloud droplets and/or raindrops) is allowed to soak and increase the bulk density if it is currently less than 900 kg m^{-3}. Collected ice crystals and snow and vapor deposition are assumed to add volume at the minimum density allowed for graupel (300 kg m^{-3}).

h. Ice initiation of graupel

Graupel can be initiated by the riming of ice crystals or snow particles. The parameterization builds on Straka and Mansell (2005) and Reisner et al. (1998) by setting a minimum rime density of 200 kg m^{-3} for conversion to graupel to occur. When rime density exceeds this threshold, the mass conversion rate is the difference between the rime accretion rate and the vapor deposition rate (qidpv):

$$\text{qgcni} = \text{qiacw} - \text{qidpv}. \quad \text{(A39)}$$

The number of particles converted is determined by the average ice or snow particle mass:

$$\text{ngcni} = \text{qgcni}\left(\frac{n_i}{q_i}\right), \quad \text{(A40)}$$

where i refers either to ice crystals or to snow particles.

i. Two-component collection

Collection of one species by another is a two-component process if the collected species is converted to the collector. Except for the specific collection processes noted below, collection of mixing ratio and number concentration of species x collecting species y take the following forms:

$$\Delta V_{x,y} = [(V_{T,x,m} - V_{T,y,m})^2 + 0.04 V_{T,x,m} V_{T,y,m}]^{1/2}, \tag{A41}$$

$$\text{qxacy} = \frac{\pi}{4} E_{x,y} n_x q_y \Delta V_{x,y} (\delta_x^0 \overline{D}_x^2 + \delta_{x,y}^1 \overline{D}_x \overline{D}_y + \delta_y^1 \overline{D}_y^2), \tag{A42}$$

$$\text{nxacy} = \frac{\pi}{4} E_{x,y} n_x n_y \Delta V_{x,y} (\delta_x^0 \overline{D}_x^2 + \delta_{x,y}^0 \overline{D}_x \overline{D}_y + \delta_y^0 \overline{D}_y^2), \tag{A43}$$

where $\Delta V_{x,y}$ is a mean fall speed difference (Murakami 1990) and the δ coefficients are functions of the shape (ν) and exponent (μ) parameters of the size distributions given by Seifert and Beheng (2006).

Accretion of cloud droplets by raindrops is treated by Eqs. (A17)–(A20). Collection of droplets or cloud ice by snow follows Zrnić et al. (1993):

$$\text{qsacy} = a_2 \epsilon E_{s,x} n_s n_y \left[\frac{(\nu_y + 2)\upsilon_y}{\nu_y + 1} + \upsilon_s \right] \left(\frac{\rho_y \overline{v}_y}{\rho_{\text{air}}} \right), \tag{A44}$$

$$\text{nsacy} = \text{qsacy} \left(\frac{\rho_{\text{air}}}{\rho_y \overline{v}_y} \right), \tag{A45}$$

where $y \rightarrow c$ for droplets and $y \rightarrow i$ for ice crystals.

j. Self-collection

Rain self-collection and breakup are treated as in Ziegler (1985). Snow aggregation is described in Zrnić et al. (1993).

k. Ice conversion to snow

Cloud ice conversion to snow is similar to Ziegler (1985), with the addition that cloud ice is two moment and therefore has a predicted mean diameter. Conversion to snow is allowed only when $\overline{D}_i > 100\ \mu$m, and the mass conversion rate is computed as a fraction of the vapor deposition rate to ice, qidpv:

$$\text{qscni} = \min \left[0.5, \left(\frac{\overline{D}_i}{\overline{D}_{s,o}} \right) \right] \text{qidpv}. \tag{A46}$$

The number of new snow particles is calculated with the assumption that the converted crystals have twice the mean crystal mass (removed from the upper tail of the distribution):

$$\text{nscni} = \text{qscni} \frac{\rho_{\text{air}}}{2 \rho_i \upsilon_i}. \tag{A47}$$

l. Graupel conversion to hail

The conversion of graupel to hail is assumed to occur when wet growth riming conditions exist. We adopt the approach of Milbrandt and Yau (2005b) to use the diameter of wet growth D_{wet} derived by Ziegler (1985) but without the use of rain content:

$$D_{\text{wet}} = 0.01 \left[\exp \left(\frac{-T_c}{1.1 \times 10^4 \rho_{\text{air}} q_c - 1.3 \times 10^3 \rho_{\text{air}} q_i + 1 \times 10^{-3}} \right) - 1 \right]. \tag{A48}$$

As in Milbrandt and Yau (2005b), the conversion rate is dependent on the sum of graupel mass growth rates, but here it is limited to removing $1/10$ of the existing graupel mass per time step:

$$\text{qhcng} = \min \left[\frac{q_g}{10 \Delta t}, \frac{\overline{D}_g}{2 D_{\text{wet}}} (\text{qhacw} + \text{qhacr} + \text{qhaci} + \text{qhacs}) \right]. \tag{A49}$$

In addition to converting only when $\overline{D}_g / D_{\text{wet}} > 0.1$ (Milbrandt and Yau 2005b), conversion is allowed only when the rime accreted by graupel has sufficiently high density ($\rho_{\text{rim},g} > 800$ kg m^{-3}). Furthermore, conversion is only allowed at temperatures $T < -2$°C to avoid spurious conversion too close to the melting level.

m. Reflectivity conservation

Following Ferrier (1994), number concentrations are adjusted to conserve reflectivity when graupel or hail melts into rain because of the differences in the distribution parameters. For $\mu_x = 1/3$ and $\mu_r = 1$,

$$R_{z,x} = \frac{(\alpha_x + 4)(\alpha_x + 5)(\alpha_x + 6)(\nu_r + 1)}{(\alpha_x + 1)(\alpha_x + 2)(\alpha_x + 3)(\nu_r + 2)}. \quad \text{(A50)}$$

Currently R_z is used only for melting of graupel and hail ($x \in \{g, h\}$), that is, to adjust the number of meltwater raindrops in order to preserve reflectivity across the melting layer. Application of this factor to raindrop freezing has an appreciable effect on electrification (increase in graupel concentration that leads to higher collision and charge separation rates), and thus is currently neglected. In the conversion of graupel to hail, the ratio $R_{z,h}/R_{z,g}$ is applied to the number of new hail particles.

APPENDIX B

List of Symbols

Symbol	Meaning/Reference	Value	Units
α	Shape parameter (diameter)	$3\nu + 2$	
γ	Fall speed factor	$(\rho_0/\rho_{\text{air}})^{1/2}$	
δ_x^0	Coefficient in collection (Seifert and Beheng 2006)		
ϵ	Collection kernel ratio (Zrnić et al. 1993)	0.104	
μ	Exponent in size distribution		
ν	Shape parameter (volume)		
ρ_{air}	Air density		kg m^{-3}
ρ_{rim}	Rime density		kg m^{-3}
ρ_0	Reference air density		kg m^{-3}
a_x	Factor in fall speed relationship		m$^{(1-b_x)}$ s^{-1}
a_i	Factor in fall speed relationship	67 057	m$^{(1-3b_i)}$ s^{-1}
a_1	Long (1974)	9.44×10^{15}	m^{-3} s^{-1}
a_2	Long (1974)	5.78×10^3	s^{-1}
A'	Constant in rain freezing (Bigg 1953)	0.66	
B'	Constant in rain freezing (Bigg 1953)	100	
b_x	Exponent in fall speed relationship		
b_i	Exponent in fall speed relationship	0.4717	
c_{r1}	Coefficient in rime density equation	300	
c_{r2}	Exponent in rime density equation	0.44	
C	Coefficient in Twomey (1959) CCN relationship		m^{-3}
C_N	Cloud droplet nucleation rate (interior)		m^{-3} s^{-1}
$C_{N,\text{cb}}$	Cloud droplet nucleation rate (cloud base)		m^{-3} s^{-1}
C_D	drag coefficient	0.45–1.0	
D	Diameter		m
$\overline{D}$	Mean volume diameter		m
$\overline{D}_{s,o}$	Snow diameter for ice → snow conversion	200×10^{-6}	m
$E_{x,y}$	Average collection efficiency of x collecting y		
$E_{s,c}$	Average collection efficiency of s collecting w	0.5	
g	Free fall acceleration	9.8	m s^{-2}
k	Exponent in Twomey (1959) CCN relationship	0.6	
L_2	Berry and Reinhardt (1974)		
n_x	Number concentration of species x		m^{-3}
n_H	Berry and Reinhardt (1974)		
N_{splint}	Number of ice splinters per frozen drop		
r_H	Berry and Reinhardt (1974)		
R	Particle radius		m
S_w	Supersaturation with respect to liquid water		%
T_0	Standard freezing temperature of water	273.15	K
$\overline{R}$	Mean volume radius		m
v	Particle volume		m^3
$\tilde{v}$	Integrated particle volume content		m^3 m^{-3}
$\overline{v}$	Mean particle volume		m^3
V_T	Terminal fall speed		m s^{-1}
$V_{T,x,m}$	Mass-weighted terminal fall speed for species x		m s^{-1}
$V_{T,x,n}$	Number-weighted terminal fall speed for species x		m s^{-1}

REFERENCES

Berry, E. X., and R. L. Reinhardt, 1974: An analysis of cloud drop growth by collection. Part II: Single initial distributions. *J. Atmos. Sci.,* **24,** 1825–1831.

Bigg, E. K., 1953: The supercooling of water. *Proc. Phys. Soc. London,* **B66,** 688–694.

Brooks, I. M., C. P. R. Saunders, R. P. Mitzeva, and S. L. Peck, 1997: The effect on thunderstorm charging of the rate of rime accretion by graupel. *Atmos. Res.,* **43,** 277–295.

Bruning, E. C., W. D. Rust, T. J. Schuur, D. R. MacGorman, P. R. Krehbiel, and W. Rison, 2007: Electrical and polarimetric radar observations of a multicell storm in TELEX. *Mon. Wea. Rev.,* **135,** 2525–2544.

Bryan, G. H., 2005: Spurious convective organization in simulated squall lines owing to moist absolutely unstable layers. *Mon. Wea. Rev.,* **133,** 1978–1997.

Chisnell, R. F., and J. Latham, 1974: A stochastic model of ice particle multiplication by drop splintering. *Quart. J. Roy. Meteor. Soc.,* **100,** 296–308.

Coleman, L. M., T. C. Marshall, M. Stolzenburg, T. Hamlin, P. R. Krehbiel, W. Rison, and R. J. Thomas, 2003: Effects of charge and electrostatic potential on lightning propagation. *J. Geophys. Res.,* **108,** 4298, doi:10.1029/2002JD002718.

——, M. Stolzenburg, T. C. Marshall, and M. Stanley, 2008: Horizontal lightning propagation, preliminary breakdown, and electric potential in New Mexico thunderstorms. *J. Geophys. Res.,* **113,** D09208, doi:10.1029/2007JD009459.

Coniglio, M. C., D. J. Stensrud, and L. J. Wicker, 2006: Effects of upper-level shear on the structure and maintenance of strong quasi-linear mesoscale convective systems. *J. Atmos. Sci.,* **63,** 1231–1252.

Cotton, W. R., G. J. Tripoli, R. M. Rauber, and E. A. Mulvihill, 1986: Numerical simulation of the effects of varying ice crystal nucleation rates and aggregation processes on orographic snowfall. *J. Climate Appl. Meteor.,* **25,** 1658–1680.

Deardorff, J. W., 1980: Stratocumulus-capped mixed layers derived from a three-dimensional model. *Bound.-Layer Meteor.,* **18,** 495–527.

Dwyer, J. R., 2003: A fundamental limit on electric fields in air. *Geophys. Res. Lett.,* **30,** 2055, doi:10.1029/2003GL017781.

Farley, R. D., 1987: Numerical modeling of hailstorms and hailstone growth. Part II: The role of low-density riming growth in hail production. *J. Climate Appl. Meteor.,* **26,** 234–254.

Ferrier, B. S., 1994: A double-moment multiple-phase four-class bulk ice scheme. Part I: Description. *J. Atmos. Sci.,* **51,** 249–280.

——, W.-K. Tao, and J. Simpson, 1995: A double-moment multiple-phase four-class bulk ice scheme. Part II: Simulations of convective storms in different large-scale environments and comparisons with other bulk parameterizations. *J. Atmos. Sci.,* **52,** 1001–1033.

Gish, O. H., 1944: Evaluation and interpretation of the columnar resistance of the atmosphere. *Terr. Magn. Atmos. Electr.,* **49,** 159–168.

Gunn, R., and G. D. Kinzer, 1949: The terminal velocity of fall for water droplets in stagnant air. *J. Meteor.,* **6,** 243–248.

Hallett, J., and S. C. Mossop, 1974: Production of secondary ice particles during the riming process. *Nature,* **249,** 26–28.

Helsdon, J. H., Jr., and R. D. Farley, 1987: A numerical modeling study of a Montana thunderstorm: 2. Model results versus observations involving electrical aspects. *J. Geophys. Res.,* **92,** 5661–5675.

——, G. Wu, and R. D. Farley, 1992: An intracloud lightning parameterization scheme for a storm electrification model. *J. Geophys. Res.,* **97,** 5865–5884.

Jiang, G.-S., and C.-W. Shu, 1996: Efficient implementation of weighted ENO schemes. *J. Comput. Phys.,* **126,** 202–228.

Kasemir, H. W., 1960: A contribution to the electrostatic theory of a lightning discharge. *J. Geophys. Res.,* **65,** 1873–1878.

Kato, T., 1995: A box-Lagrangian rain-drop scheme. *J. Meteor. Soc. Japan,* **73,** 241–245.

Klemp, J. B., and R. B. Wilhelmson, 1978a: Simulations of right- and left-moving storms produced through storm splitting. *J. Atmos. Sci.,* **35,** 1097–1110.

——, and ——, 1978b: The simulations of three-dimensional convective storm dynamics. *J. Atmos. Sci.,* **35,** 1070–1096.

Krehbiel, P. R., 1986: The electrical structure of thunderstorms. *The Earth's Electrical Environment,* National Acadamies Press, 90–113.

——, J. A. Riousset, V. P. Pasko, R. J. Thomas, W. Rison, M. A. Stanley, and H. E. Edens, 2008: Upward electrical discharges from thunderstorms. *Nature Geosci.,* **1,** 233–237.

Leonard, B. P., 1991: The ULTIMATE conservative difference scheme applied to unsteady one-dimensional advection. *Comput. Methods Appl. Mech. Eng.,* **88,** 17–74.

Long, A. B., 1974: Solutions to the droplet collection equation for polynomial kernels. *J. Atmos. Sci.,* **31,** 1040–1052.

MacGorman, D. R., A. A. Few, and T. L. Teer, 1981: Layered lightning activity. *J. Geophys. Res.,* **86,** 9900–9910.

——, J. M. Straka, and C. L. Ziegler, 2001: A lightning parameterization for numerical cloud models. *J. Appl. Meteor.,* **40,** 459–478.

——, and Coauthors, 2008: TELEX The thunderstorm electrification and lightning experiment. *Bull. Amer. Meteor. Soc.,* **89,** 997–1013.

Mansell, E. R., D. R. MacGorman, C. L. Ziegler, and J. M. Straka, 2002: Simulated three-dimensional branched lightning in a numerical thunderstorm model. *J. Geophys. Res.,* **107,** 4075, doi:10.1029/2000JD000244.

——, ——, ——, and ——, 2005: Charge structure and lightning sensitivity in a simulated multicell thunderstorm. *J. Geophys. Res.,* **110,** D12101, doi:10.1029/2004JD005287.

Marshall, T. C., M. P. McCarthy, and W. D. Rust, 1995: Electric field magnitudes and lightning initiation in thunderstorms. *J. Geophys. Res.,* **100,** 7097–7103.

Mazur, V., 2002: Physical processes during the development of lightning flashes. *C. R. Phys.,* **3,** 1393–1409.

——, and L. H. Ruhnke, 1998: Model of electric charges in thunderstorms and associated lightning. *J. Geophys. Res.,* **103,** 23 299–23 308.

Meyers, M. P., P. J. DeMott, and W. R. Cotton, 1992: New primary ice-nucleation parameterizations in an explicit cloud model. *J. Appl. Meteor.,* **31,** 708–721.

Milbrandt, J. A., and M. K. Yau, 2005a: A multimoment bulk microphysics parameterization. Part I: Analysis of the role of the spectral shape parameter. *J. Atmos. Sci.,* **62,** 3051–3064.

——, and ——, 2005b: A multimoment bulk microphysics parameterization. Part II: A proposed three-moment closure and scheme description. *J. Atmos. Sci.,* **62,** 3065–3081.

Mitzeva, R., C. Saunders, and B. Tsenova, 2006: Parameterisation of non-inductive charging in thunderstorm regions free of cloud droplets. *Atmos. Res.,* **82,** 102–111, doi:10.1016/j.atmosres.2005.12.006.

Murakami, M., 1990: Numerical modeling of dynamical and microphysical evolution of an isolated convective cloud—The 19 July CCOPE cloud. *J. Meteor. Soc. Japan,* **68,** 107–128.

Qie, X., T. Zhang, C. Chen, G. Zhang, T. Zhang, and W. Wei, 2005: The lower positive charge center and its effect on lightning discharges on the Tibetan Plateau. *Geophys. Res. Lett.,* **32,** L05814, doi:10.1029/2004GL022162.

Rasmussen, R. M., and A. J. Heymsfield, 1985: A generalized form for impact velocities used to determine graupel accretional densities. *J. Atmos. Sci.,* **42,** 2275–2279.

Reisner, J., R. M. Rasmussen, and R. T. Bruintjes, 1998: Explicit forcasting of supercooled liquid water in winter storms using the MM5 mesoscale model. *Quart. J. Roy. Meteor. Soc.,* **124,** 1071–1107.

Riousset, J. A., V. P. Pasko, P. R. Krehbiel, R. J. Thomas, and W. Rison, 2007: Three-dimensional fractal modeling of intracloud lightning discharge in a New Mexico thunderstorm and comparison with lightning mapping observations. *J. Geophys. Res.,* **112,** D15203, doi:10.1029/2006JD007621.

Saunders, C. P. R., and S. L. Peck, 1998: Laboratory studies of the influence of the rime accretion rate on charge transfer during crystal/graupel collisions. *J. Geophys. Res.,* **103,** 13 949–13 956.

——, W. D. Keith, and R. P. Mitzeva, 1991: The effect of liquid water on thunderstorm charging. *J. Geophys. Res.,* **96,** 11 007–11 017.

Seifert, A., and K. D. Beheng, 2006: A two-moment cloud microphysics parameterization for mixed-phase clouds. Part 1: Model description. *Meteor. Atmos. Phys.,* **92,** 45–66, doi:10.1007/s00703-005-0112-4.

Shu, C.-W., 2003: High-order finite difference and finite volume WENO schemes and discontinuous Galerkin methods for CFD. *Int. J. Comput. Fluid Dyn.,* **17,** 107–118.

Straka, J. M., and E. R. Mansell, 2005: A bulk microphysics parameterization with multiple ice precipitation categories. *J. Appl. Meteor.,* **44,** 445–466.

Tan, Y., S. Tao, and B. Zhu, 2006: Fine-resolution simulation of the channel structures and propagation features of intracloud lightning. *Geophys. Res. Lett.,* **33,** L09809, doi:10.1029/2005GL025523.

Twomey, S., 1959: The nuclei of natural cloud formation. Part II: The supersaturation in natural clouds and the variation of cloud droplet concentration. *Geofis. Pura Appl.,* **43,** 243–249.

Wacker, U., and A. Seifert, 2001: Evolution of rain water profiles resulting from pure sedimentation: Spectral vs. parameterized description. *Atmos. Res.,* **58,** 19–39.

Wicker, L. J., and R. B. Wilhelmson, 1995: Simulation and analysis of tornado development and decay within a three-dimensional supercell thunderstorm. *J. Atmos. Sci.,* **52,** 2675–2703.

——, and W. C. Skamarock, 2002: Time-splitting methods for elastic models using forward time schemes. *Mon. Wea. Rev.,* **130,** 2088–2097.

Wiens, K. C., S. A. Rutledge, and S. A. Tessendorf, 2005: The 29 June 2000 supercell observed during STEPS. Part II: Lightning and charge structure. *J. Atmos. Sci.,* **62,** 4151–4177.

Wilson, C. T. R., 1921: Investigations on lightning discharges and on the electric field of thunderstorms. *Philos. Trans. Roy. Soc. London,* **A221,** 73–115.

Wisner, C., H. D. Orville, and C. Meyers, 1972: A numerical model of a hail-bearing cloud. *J. Atmos. Sci.,* **29,** 1160–1181.

Xue, M., 2000: High-order monotonic numerical diffusion and smoothing. *Mon. Wea. Rev.,* **128,** 2853–2864.

Ziegler, C. L., 1985: Retrieval of thermal and microphysical variables in observed convective storms. Part I: Model development and preliminary testing. *J. Atmos. Sci.,* **42,** 1487–1509.

——, and D. R. MacGorman, 1994: Observed lightning morphology relative to modeled space charge and electric field distributions in a tornadic storm. *J. Atmos. Sci.,* **51,** 833–851.

——, P. S. Ray, and D. R. MacGorman, 1986: Relations of kinematics, microphysics and electrification in an isolated mountain thunderstorm. *J. Atmos. Sci.,* **43,** 2098–2114.

——, D. R. MacGorman, J. E. Dye, and P. S. Ray, 1991: A model evaluation of non-inductive graupel-ice charging in the early electrification of a mountain thunderstorm. *J. Geophys. Res.,* **96,** 12 833–12 855.

Zrnić, D. S., N. Balakrishnan, C. L. Ziegler, V. N. Bringi, K. Aydin, and T. Matejka, 1993: Polarimetric signatures in the stratiform region of a mesoscale convective system. *J. Appl. Meteor.,* **32,** 678–693.